CORONAVIRUS

An ACE2-blocking antibody confers broad neutralization and protection against Omicron and other SARS-CoV-2 variants of concern

Wenjuan Du[1], Daniel L. Hurdiss[1], Dubravka Drabek[2,3], Anna Z. Mykytyn[4], Franziska K. Kaiser[5], Mariana González-Hernández[5], Diego Muñoz-Santos[6], Mart M. Lamers[4], Rien van Haperen[2,3], Wentao Li[1]†, Ieva Drulyte[7], Chunyan Wang[1], Isabel Sola[6], Federico Armando[8], Georg Beythien[8], Malgorzata Ciurkiewicz[8], Wolfgang Baumgärtner[8], Kate Guilfoyle[9], Tony Smits[1], Joline van der Lee[1], Frank J. M. van Kuppeveld[1], Geert van Amerongen[9], Bart L. Haagmans[4], Luis Enjuanes[6], Albert D. M. E. Osterhaus[5,10], Frank Grosveld[2,3], Berend-Jan Bosch[1]*

The ongoing evolution of SARS-CoV-2 has resulted in the emergence of Omicron, which displays notable immune escape potential through mutations at key antigenic sites on the spike protein. Many of these mutations localize to the spike protein ACE2 receptor binding domain, annulling the neutralizing activity of therapeutic antibodies that were effective against other variants of concern (VOCs) earlier in the pandemic. Here, we identified a receptor-blocking human monoclonal antibody, 87G7, that retained potent in vitro neutralizing activity against SARS-CoV-2 variants including the Alpha, Beta, Gamma, Delta, and Omicron (BA.1/BA.2) VOCs. Using cryo–electron microscopy and site-directed mutagenesis experiments, we showed that 87G7 targets a patch of hydrophobic residues in the ACE2-binding site that are highly conserved in SARS-CoV-2 variants, explaining its broad neutralization capacity. 87G7 protected mice and hamsters prophylactically against challenge with all current SARS-CoV-2 VOCs and showed therapeutic activity against SARS-CoV-2 challenge in both animal models. Our findings demonstrate that 87G7 holds promise as a prophylactic or therapeutic agent for COVID-19 that is more resilient to SARS-CoV-2 antigenic diversity.

INTRODUCTION

Since its emergence in humans in late 2019, severe acute respiratory syndrome coronavirus 2 (SARS-CoV-2) has caused >500 million infections and >6.2 million confirmed deaths worldwide. This massive propagation has allowed rapid evolution of the virus, leading to the independent emergence of a multitude of variants beginning in late 2020. Five of these have been declared by the World Health Organization as variants of concern (VOCs)—B.1.1.7 (Alpha), B.1.351 (Beta), P.1 (Gamma), B.1.617.2 (Delta), and B.1.1.529 (Omicron; main subvariants BA.1 and BA.2)—because they display increased transmission, immune evasion, and/or enhanced disease. Other variants that have spread less widely, but with mutations similar to those present within VOCs, have been defined as variants of interest (VOIs) such as C.37 (Lambda) and B.1.621 (Mu) (*1*). Some SARS-CoV-2 variants—in particular, Beta, Gamma, and Omicron—have accrued mutations in the spike (S) protein that correlate with escape from humoral immunity. Sera from patients infected with the ancestral strain and sera from coronavirus disease 2019 (COVID-19) vaccinees exhibit 3- to 9-fold reductions in neutralization activity against Beta and Gamma (*1*–*3*), whereas neutralizing activity against the globally emerging Omicron is reduced to about 25- to 40-fold (*4*–*11*). With global population seroprevalence increasing due to natural infection and/or vaccination, the ongoing evolution of SARS-CoV-2 may lead to the continuous emergence of antigenically drifted variants that jeopardize the effectiveness of vaccines and antibody-based therapeutics.

Entry of SARS-CoV-2 into host cells is mediated by the trimeric S glycoprotein that consists of two subunits: S1 and S2. The S1 subunit binds the host angiotensin-converting enzyme 2 (ACE2) receptor, and the S2 subunit accomplishes membrane fusion. The N-terminal domain (NTD) and the receptor binding domain (RBD), within the S1 subunit, are the major targets of neutralizing antibodies. These domains are hotspots for mutations observed in SARS-CoV-2 variants that enable escape of serum neutralizing antibodies from infected or vaccinated individuals and of NTD- and RBD-directed monoclonal antibodies (mAbs). Escape mutations in the RBD are concentrated in the four major and structurally defined neutralizing epitope classes in the RBD (*12*). In particular, the S proteins of the emerging Omicron BA.1 and BA.2 subvariants carry an unprecedented set of mutations (about 30 substitutions, deletions, or insertions) with amino acid substitutions in each of these neutralizing epitope classes, including K417N (class 1), E484A (class 2), G446V (class 3), and G339D (class 4), as well as mutations in the major neutralizing epitope in the NTD (e.g., G142D and deletion of residues 143 to 145, NTD supersite), potentiating viral escape from vaccine- and infection-elicited antibody-mediated immunity (*5*, *13*–*16*). The escape mutations also have a devastating effect on neutralization by

[1]Virology Section, Infectious Diseases and Immunology Division, Department of Biomolecular Health Sciences, Faculty of Veterinary Medicine, Utrecht University, Utrecht, Netherlands. [2]Department of Cell Biology, Erasmus Medical Center, Rotterdam, Netherlands. [3]Harbour BioMed, Rotterdam, Netherlands. [4]Department of Viroscience, Erasmus Medical Center, Rotterdam, Netherlands. [5]Research Center for Emerging Infections and Zoonoses, University of Veterinary Medicine Hannover, Foundation, Hannover, Germany. [6]Department of Molecular and Cell Biology, National Center for Biotechnology-Spanish National Research Council (CNB-CSIC), Madrid, Spain. [7]Thermo Fisher Scientific, Materials and Structural Analysis, Eindhoven, Netherlands. [8]Department of Pathology, University of Veterinary Medicine Hannover, Foundation, Hannover, Germany. [9]Viroclinics Xplore, Schaijk, Netherlands. [10]Global Virus Network, Center of Excellence, Baltimore, MD, USA.
*Corresponding author. Email: b.j.bosch@uu.nl
†Present address: State Key Laboratory of Agricultural Microbiology, College of Veterinary Medicine, Huazhong Agricultural University, Wuhan, P.R. China.

the potent neutralizing ACE2-blocking antibodies corresponding to those that are emergency use authorized for the treatment of COVID-19. REGN10933 and REGN10987 (Regeneron) and LY-CoV555 and LY-CoV016 (Eli Lilly) completely lost neutralization of Omicron, whereas COV2-2130 and COV2-2196 (parent mAbs of AZD1061 and AZD8895, AstraZeneca) show an intermediate 12- to 428-fold and 74- to 197-fold loss in neutralization potential against BA.1 Omicron, respectively (*5*, *15*, *17*–*22*). Of the clinically approved or authorized antibodies, S309 (parent of the clinical mAb VIR-7831, Vir Biotechnology) retains substantial neutralization against BA.1 Omicron (2- to 3-fold potency loss), but its potency is substantially reduced against BA.2 Omicron (27-fold potency loss) (*5*, *15*, *17*–*22*). In general, Omicron escapes existing SARS-CoV-2–neutralizing antibodies with few exceptions, which has major consequences for antibody-based treatment strategies for COVID-19 (*5*, *15*, *17*–*21*, *23*). Isolation and in-depth characterization of broadly neutralizing and protective antibodies can inform the development of improved vaccines and mAb treatments for COVID-19 that are more resistant to antigenically drifted SARS-CoV-2 variants.

Here, we identified a SARS-CoV-2–neutralizing human mAb, 87G7, with a remarkable broad-spectrum neutralization and protection efficacy. 87G7 blocked SARS-CoV-2 infection via ACE2 binding inhibition with robust neutralizing activity against Alpha, Beta, Gamma, Delta, and Omicron. Structural elucidation revealed that 87G7 could bind the highly divergent ACE2 receptor binding site by targeting a patch of hydrophobic residues in the convex tip of the receptor binding ridge (RBR) that are highly conserved in SARS-CoV-2 variants, including the five VOCs. We demonstrated in vivo prophylactic and therapeutic activity by 87G7 against ancestral and variant SARS-CoV-2 using two animal disease models. Hence, by binding to a conserved epitope in the S protein receptor binding site, 87G7 provides potent neutralization and broad protection against antigenically drifted SARS-CoV-2 variants.

RESULTS

Human mAb 87G7 potently neutralizes Omicron and other VOCs/VOIs

To identify human mAbs with broad neutralizing capacity against SARS-CoV-2 variants, we explored the antibody repertoire of Harbour H2L2 mice immunized with the SARS-CoV-2 S protein. The transgenic H2L2 mice encoding chimeric immunoglobulins (Igs) with human variable heavy (VH) and variable light (VL) chains and murine constant region were immunized with plasmid DNA encoding the S ectodomain and with purified trimeric S ectodomain of the ancestral SARS-CoV-2 strain Wuhan-Hu-1 (fig. S1A). Hybridoma supernatants with S ectodomain enzyme-linked immunosorbent assay (ELISA) reactivity were screened for neutralizing activity against SARS-CoV-2 S pseudo-virus with the S E484K mutation, a residue that is at variance in several SARS-CoV-2 VOIs and VOCs playing a key role in resistance to neutralizing antibodies (Fig. 1A) (*5*, *14*, *15*, *17*). Among the ~300 hybridoma supernatants tested, the 87G7 hybridoma supernatant displayed the most potent neutralizing activity (fig. S1B). The chimeric 87G7 H2L2 antibody was subsequently converted to a fully human Ig, by cloning of the human VH and VL chain regions into a human IgG1/kappa chain backbone, and the recombinantly expressed 87G7 human mAb was evaluated for its capacity to neutralize the prototypic Wuhan-Hu-1 SARS-CoV-2 and the Alpha, Beta, Delta, and Omicron VOCs using the vesicular stomatitis virus (VSV) pseudo-virus neutralization assay. Two therapeutic mAbs, REGN10933 and REGN10987, were used for comparison (*24*). 87G7 exhibited potent neutralizing efficacy against Wuhan-Hu-1 S–mediated cell entry with a half-maximum inhibitory concentration (IC_{50}) of 5.4 ng/ml. In addition, entry of VSV pseudotypes harboring S proteins from VOCs including Alpha, Beta, Delta, and Omicron (BA.1 subvariant) was blocked with IC_{50} values ranging from 1.4 to 5.1 ng/ml. REGN10933 showed decreased neutralization potency against Beta and Omicron, corresponding with a 20- and 350-fold loss in IC_{50}, respectively, whereas neutralization potential against Omicron by REGN10987 was lost (Fig. 1, B and E). Neutralization potency of 87G7 and REGN10933 was subsequently tested in live virus neutralization assay. Relative to an early pandemic strain with D614G S mutation (D614G), REGN10933 exhibited a fold loss in inhibitory activity of 7.8 and 15.9 against Beta and Gamma, respectively, and had fully lost its neutralization potential against Omicron BA.1. In contrast, 87G7 potently neutralized D614G (IC_{50}, 5.7 ng/ml), as well as Alpha, Beta, Gamma, Delta, and Omicron (subvariants BA.1 and BA.2) VOCs with IC_{50} values ranging from 3.1 to 12.5 ng/ml (Fig. 1, C and E). In addition, 87G7 neutralized Lambda and Mu VOIs with similar potency (IC_{50} values: 1.2 and 4.8 ng/ml, respectively) to D614G (Fig. 1, D and E).

We next evaluated the epitope location and mechanism of action of 87G7. The antibody bound to the S RBD as demonstrated by ELISA using different SARS-CoV-2 S antigen forms (fig. S2A). By using biolayer interferometry (BLI), 87G7 IgG showed strong, subnanomolar affinity against monomeric S1 and picomolar apparent binding affinity against trimeric S ectodomain, suggesting bivalent binding to the S trimer (fig. S2B). Binding competition of 87G7 with published mAbs targeting distinct RBD epitopes was determined by BLI. Binding interference for 87G7 was only seen with the class 1 antibody REGN10933, indicating an overlapping binding epitope on the RBD (fig. S2C). To understand the mechanism of virus neutralization, we assessed the antibody interference with S-mediated receptor binding activity. Similar to REGN10933, 87G7 was found to block the binding of recombinant S trimer to ACE2, as shown by BLI and ELISA-based assay, rationalizing the potent neutralizing activity by 87G7 (fig. S2, D and E).

Structural basis for broad neutralization by 87G7

To understand the structural basis for 87G7-mediated neutralization of SARS-CoV-2, we performed cryo–electron microscopy (cryo-EM) analysis on the 6P-stabilized SARS-CoV-2 S trimer (*25*) in complex with the 87G7 Fab fragment (fig. S3, A to D, and table S1). Three-dimensional (3D) classification of the data revealed that the S ectodomains had all three RBDs in the open conformation with the 87G7 Fab fragment bound to the flexible, convex tip of the RBR. Subsequent 3D refinement produced a density map with a global resolution of 2.9 Å (Fig. 2A and fig. S3, E to G). Because of the conformational dynamics of the RBD and the flexible nature of the RBR, the epitope-paratope region was poorly resolved. To improve the interpretation of the 87G7 binding site, focused refinement was performed on the Fab-RBD region of the density map, which improved the local resolution sufficiently to approximate the positions of bulky side chains, which make up the majority of the epitope-paratope interface (fig. S3H). Consistent with our BLI data, the 87G7 epitope overlapped with the ACE2 binding site, preventing receptor engagement through steric hindrance (Fig. 2B). The 87G7 core epitope appeared to consist of residues Y421, L455, F456, F486, and Y489, which formed a

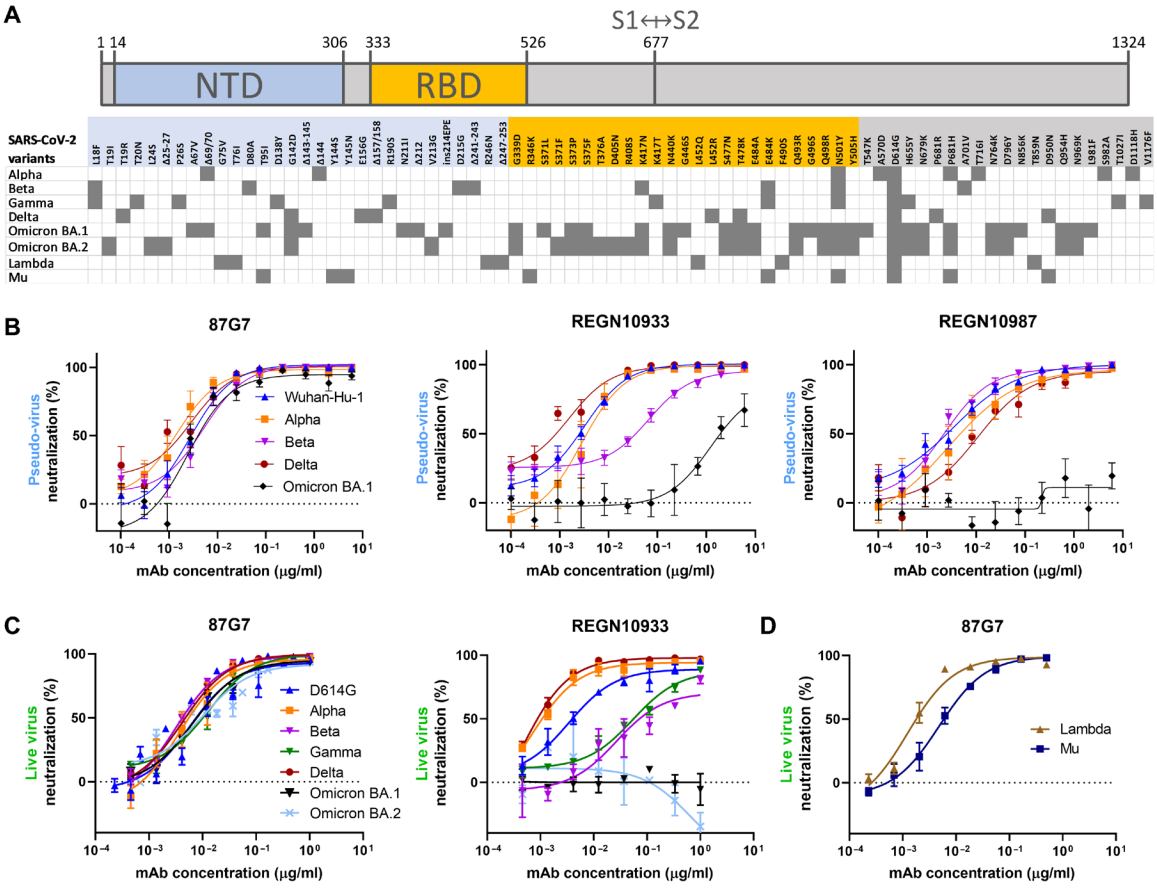

E

	Original	Alpha	Beta	Gamma	Delta	Omicron BA.1	Omicron BA.2	Lambda	Mu
	Pseudo-virus neutralization (IC_{50}: ng/ml)								
87G7	2.7	1.4	5.1	NT	2.9	2.4	NT	NT	NT
REGN10933	3.2	2.8	66.9	NT	1.5	1229	NT	NT	NT
REGN10987	4.7	4.0	2.3	NT	10.5	>6000	NT	NT	NT
	Live virus neutralization (IC_{50}: ng/ml)								
87G7	5.7	3.7	3.1	12.5	4.2	6.7	10.2	1.2	4.8
REGN10933	3.4	0.7	26.4	54	0.4	>1000	>1000	NT	NT

Fig. 1. 87G7 potently neutralizes Omicron and other SARS-CoV-2 variants. (**A**) S protein schematic with mutations indicated that are found in Alpha, Beta, Gamma, Delta, and Omicron (BA.1 and BA.2) VOCs and Lambda and Mu VOIs, relative to ancestral SARS-CoV-2. The S NTD (in blue), RBD (in orange), and S1/S2 junction are indicated. (**B**) Neutralizing activity of 87G7 against virus particles pseudo-typed with ancestral SARS-CoV-2 S (Wuhan-Hu-1 strain) or S proteins of Alpha, Beta, Delta, and Omicron. Error bars indicate SD between at least two independent replicates. (**C** and **D**) 87G7-mediated neutralization of live SARS-CoV-2 and variants. Neutralizing potency of 87G7 and REGN10933 against the D614G SARS-CoV-2 and Alpha, Beta, Delta, Gamma, and BA.1 and BA.2 Omicron VOCs (C) and against Lambda and Mu SARS-CoV-2 VOIs (D). Error bars indicate SD between at least two independent replicates. (**E**) IC_{50} values of 87G7 against SARS-CoV-2 variants calculated from the neutralization curves displayed in (B) to (D). NT, not tested.

hydrophobic patch on the RBD (Fig. 2C). The interaction between 87G7 and the RBR was primarily mediated by the complementarity-determining region (CDR) H2 and H3 and CDR L1 and L3 loops, which formed a hydrophobic interface. RBD residues F486 and Y489 inserted into a hydrophobic cleft formed by the side chains of CDR H2-3 residues Y59 and Y103, Y104, and CDR L3 residues F92 and W94. This interaction is reminiscent of the RBD-ACE2 interaction, where F486 penetrates a deep hydrophobic pocket formed by receptor residues F28, L79, Y83, and L97 (Fig. 2D). Additional residues outside of the core epitope-paratope interface may also contribute to the interaction between 87G7 and the RBD but were not interpreted further because of limited resolution in these areas.

To verify the 87G7 epitope, we evaluated the relative contribution of predicted contact residues on antibody binding. Consistent with the structural data, the F486A mutation strongly reduced 87G7 S binding activity in ELISA (Fig. 2E). F486A also blocked binding by REGN10933, whereas it had no effect on REGN10987 binding, which is consistent with their reported epitopes (*24*). Alanine substitution of Y489 prevented binding by all three antibodies. F456A mutation only slightly impaired binding by 87G7, whereas a stronger reduction in binding was observed for REGN10933 and REGN10987. We assessed the impact of these alanine substitutes in neutralization escape using the pseudo-virus system. Pseudo-virus production for S^{F456A} and S^{Y489A}, however, did not yield infectious virus, consistent

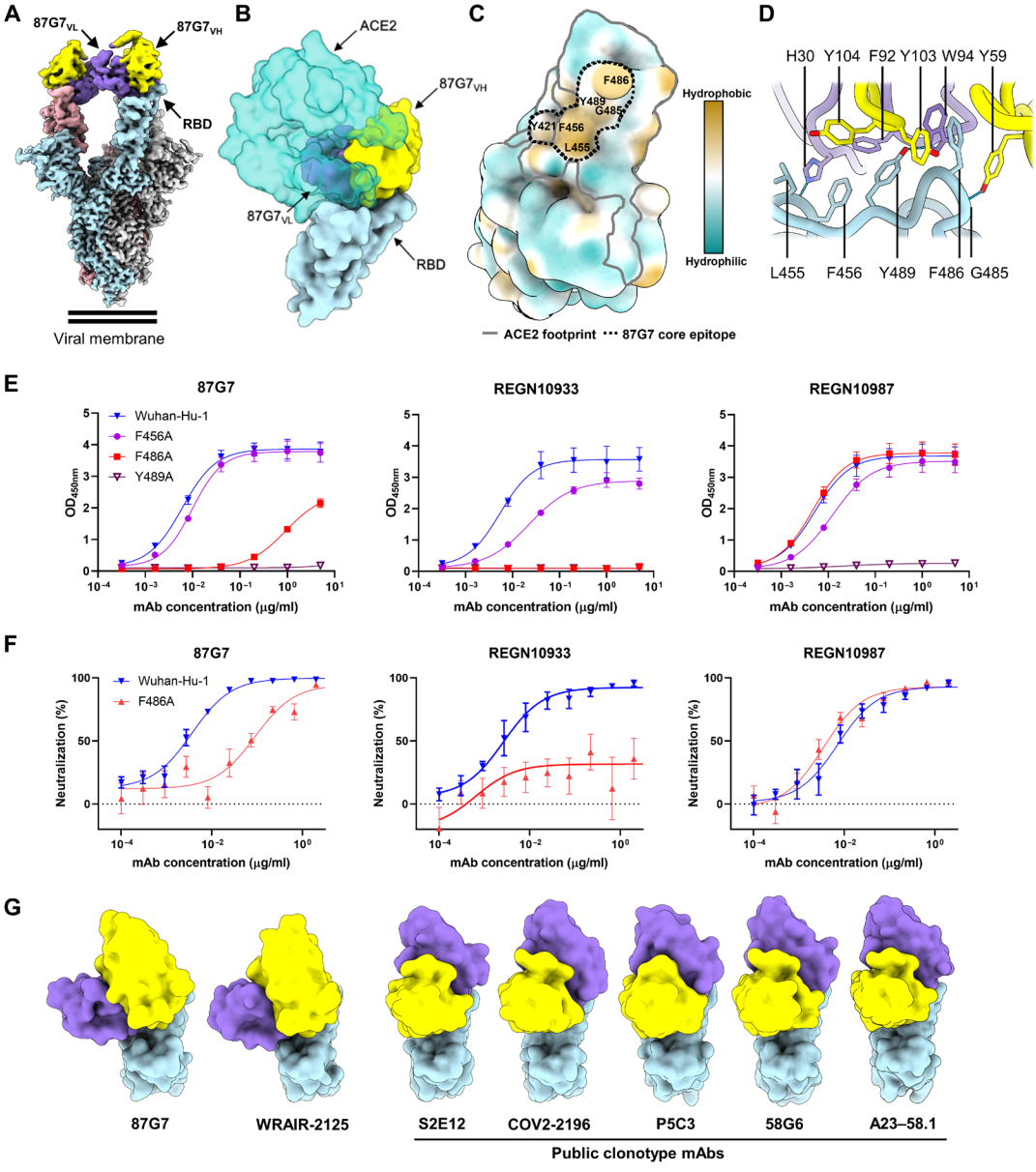

H

mAb	Heavy chain			HCDR3	Light chain		LCDR3	PDB	Reference
	V gene	D gene	J gene		V gene	J gene			
87G7	IGHV3-23*01	IGHD3-10*01	IGHJ5*02	AKEGTYYYGSGSF	IGKV3-11*01	IGKJ4*01	QQRFNWPLT	7R40	This study
WRAIR-2125	IGHV3-30*18	IGHD3-22*01	IGHJ1*01	AKDSPYYYDSSGYYPGYFQD	IGKV1-39*01	IGKJ1*01	QQSYITPRT	7N4L	[33]
S2E12	IGHV1-58*01	IGHD2-15*01	IGHJ3*02	ASPYCSGGSCSDGFDI	IGKV3-20*01	IGKJ1*01	QQYVGLTGWT	7K45	[28]
COV2-2196	IGHV1-58*01	IGHD2-2*01	IGHJ3*02	AAPYCSSISCNDGFDI	IGKV3-20*01	IGKJ1*01	QHYGSSRGWT	7L7D	[32]
2C08	IGHV1-58*01	IGHD2-15*01	IGHJ3*02	AAAYCSGGSCSDGFDI	IGKV3-20*01	IGKJ1*01	QQYGSSPWT	NA	[27]
P5C3	IGHV1-58*01	IGHD2-15*01	IGHJ2*01	AAPNCSGGSCYDGFDL	IGKV3-20*01	IGKJ1*01	QQYGSSPWT	7PHG	[30]
58G6	IGHV1-58*01	IGHD2-2*01	IGHJ3*02	AAPNCNSTTCHDGFDI	IGKV3-20*01	IGKJ1*01	QQYDNSPWT	7E3L	[29]
A23–58.1	IGHV1-58*01	IGHD2-8*01	IGHJ6*02	AAPNCSNVVCYDGFDI	IGKV3-20*01	IGKJ1*01	QQYGTSPWT	7LRS	[31]

Fig. 2. Structural basis for binding and neutralization by 87G7. (**A**) Composite cryo-EM density map for the SARS-CoV-2 S ectodomain in complex with the 87G7 antibody Fab fragment. The S protomers are colored blue, gray, and pink and the 87G7 LC and HC variable domains colored purple and yellow, respectively. (**B**) Surface representation of the 87G7-bound RBD overlaid with the RBD-bound ACE2 (PDB ID: 6M0J). (**C**) Surface representation of the RBD colored according to the Kyte-Doolittle scale, where the most hydrophobic residues are colored tan, and the most hydrophilic residues are colored blue. The residues that make up the 87G7 core epitope and the ACE2 footprint are outlined. (**D**) Close-up view showing selected interactions formed between 87G7 and the SARS-CoV-2 RBD. (**E**) ELISA binding of 87G7 to plate-immobilized wild-type (WT), F456A, F486A, and Y489A S1 domains. (**F**) 87G7 neutralizing activity against pseudo-viruses with Wuhan-Hu-1 S and S^{F486A}. REGN10933 and REGN10987 were taken along as a reference in (E) and (F). (**G**) Side-by-side comparison of the SARS-CoV-2 RBD bound to 87G7, WRAIR-2125 (PDB ID: 7N4L), 58G6 (PDB ID: 7E3L), P5C3 (PDB ID: 7PHG), COV2-2196 (PDB ID: 7L7D), S2E12 (PDB ID: 7K45), and A23-58.1 (PDB ID: 7LRS). (**H**) Germline origins and CDR3 sequences of HC and LC of 87G7 and other F486-directed SARS-CoV-2 mAbs with broad neutralization capacity. PDB entries of S-antibody structures and references are indicated. NA, not applicable; OD_{450nm}, optical density at 450 nm.

with the reported unfavorable impact of these alanine substitutions on ACE2 binding (*26*). The S^{F486A} mutant pseudo-virus was inefficiently neutralized by 87G7 (and by REGN10933) (Fig. 2F), mirroring the ELISA binding data and confirming that F486 is a key residue for 87G7 binding and neutralization.

We next made a structural comparison with other broadly neutralizing mAbs that bind the RBD epitopes with F486 as a key central residue (2C08, 58G6, COV2-2196, P5C3, S2E12, and A23-58.1) (*27*–*32*). The orientations of these molecules are highly similar, with each binding parallel to the longest axis of the ACE2 binding site and the antibody light chain sitting atop the convex tip of the RBR (Fig. 2G). These antibodies are derived from different donors but share Ig heavy (IGHV1-58)– and light (IGKV3-20)–chain germline origins and display high sequence identity (Fig. 2H), indicating a public B cell clone (public clonotype) (*27*). These six public clonotype antibodies potently neutralize Alpha, Beta, Gamma, and Delta.

Two of them, S2E12 and COV2-2196, have been assessed thus far for Omicron neutralization and exhibit a loss in IC_{50} of 242 (in pseudo-virus assay) and 74- to 197-fold (in live virus assay), respectively (*5*, *15*, *17*, *20*, *22*). Although 87G7 bound an overlapping epitope that is functionally similar, it had distinct structural and genetic features. First, 87G7 bound perpendicular to the RBR and was rotated ~122° relative to these other antibodies. Second, the ancestral germ lines were different, and the heavy and light chains had the IGHV3-23 and IGKV3-11 germline origins, respectively. Another F486-targeting antibody, WRAIR-2125, with broad neutralization potential against Alpha, Beta, Gamma, and Delta encoded from distinct heavy-chain (IGHV3-30*18) and light-chain (IGKV1-39*01) germline genes has been reported (*33*). Despite originating from different germline genes, the binding mode is similar for WRAIR-2125 and 87G7 (Fig. 2E). However, there are differences in the epitope-paratope interactions between these two antibodies. For example, the CDR H3 loop of WRAIR-2125, which is partially disordered in the Fab-RBD crystal structure, is orientated away from the RBR. In contrast, the shorter CDR H3 loop of 87G7 adopted a conformation that placed Y103 between F486 and Y489. In addition, the CDR L3 loop of WRAIR-2125 interacted with F486 via T94, whereas the equivalent residue in 87G7 was a tryptophan, creating the possibility for aromatic stacking interactions. Collectively, the side chains of 87G7 residues Y59 (CDR H2), Y103 (CDR H3), and W94 (CDR L3) created a deep, F486-binding pocket that is not present in WRAIR-2125 (fig. S4, A and B). Thus far, WRAIR-2125 has not been assessed for Omicron neutralization.

The 87G7 core epitope residues Y421, L455, F456, F486, and Y489 are highly conserved among SARS-CoV-2 variants (Fig. 3A). Mutations at these residue positions occur at a very low frequency

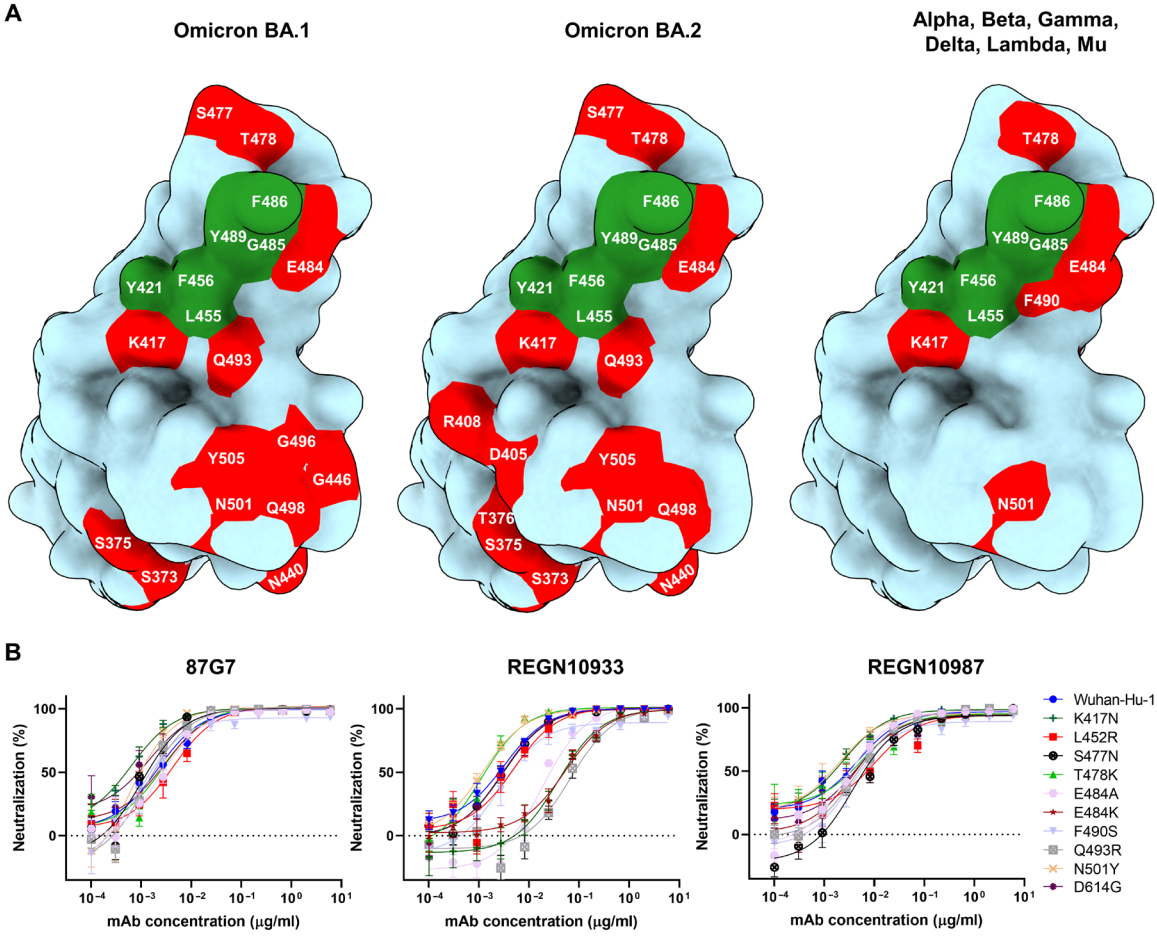

	Pseudo-virus neutralization (IC_{50}:ng/ml)										
	WT	K417N	L452R	S477N	T478K	E484A	E484K	F490S	Q493R	N501Y	D614G
87G7	2.1	0.6	4.9	1.0	2.8	2.4	2.9	0.9	1.2	0.6	1.0
REGN10933	3.2	38	5.0	3.0	1.1	18.2	53.2	2.6	67	1.2	3.0
REGN10987	4.7	3.0	10.5	3.8	5.9	2.7	3.9	3.5	4.3	2.0	4.6

Fig. 3. 87G7 recognizes a conserved epitope in SARS-CoV-2 RBD. (**A**) Surface representation of the SARS-CoV-2 S RBD with mutations colored red that are found in Omicron BA.1 (left) and Omicron BA.2 (middle). The right displays the set of mutations surrounding the 87G7 core epitope that are present in Alpha, Beta, Gamma, Delta, Lambda, or Mu (see also Fig. 1A). The 87G7 core epitope residues are colored green. (**B**) 87G7 neutralizing activity against pseudo-viruses with S variants carrying single-residue substitutions found in the SARS-CoV-2 VOCs. The REGN10933 and REGN10987 therapeutic mAbs were used for benchmarking. Data are shown as means (± SEM) of two independent experiments with technical triplicates, and corresponding IC_{50} titers are presented in the bottom.

(<0.05%) of human-derived SARS-CoV-2 sequences on GISAID as of 5 February 2022. The ACE2 interaction site, however, comprises a notable number of residues that are mutated in SARS-CoV-2 variants, of which some—including K417N, L452R, S477N, T478K, E484A, E484K, F490S, and Q493R—are close to the 87G7 core epitope and may increase ACE2 affinity and/or enable antibody escape (*24*, *26*, *34*). The Q493R mutation falls within the calculated footprint of the public clonotype mAb, COV2-2196, and may partially explain its reduced neutralization efficacy against Omicron but not earlier variants (fig. S5, A to C) (*15*, *17*, *18*, *20*, *22*). We measured the neutralization potential of 87G7 against pseudo-viruses carrying S proteins with single-site RBD mutations found in VOCs/VOIs. In contrast to REGN10933, 87G7 displayed potent neutralization against all S mutations tested, which is consistent with the ability of 87G7 to retain potent neutralization against the SARS-CoV-2 variants (Fig. 3B) (*24*).

87G7 provides in vivo protection from challenge with D614G and SARS-CoV-2 variants

The in vivo protection capacity of 87G7 against SARS-CoV-2 challenge was first evaluated using the K18-hACE2 transgenic mouse model. To assess prophylactic activity, mice were intraperitoneally injected with 87G7 (10 mg/kg of body weight) or an IgG1 isotype control (10 mg/kg) and challenged intranasally 16 hours later with 10^5 plaque-forming units (PFU) of SARS-CoV-2 using the D614G strain and Alpha, Beta, Gamma, or Delta VOCs (the Omicron VOC was not included here because it had not emerged at the time this experiment was performed). Mice were scored for weight loss, and lungs were collected at day 5 after challenge for quantification of lung antigen levels and infectious virus. Animals in isotype-treated groups started losing weight after 2 days (Alpha and Gamma), 3 days (D614G and Beta), or 4 days (Delta) after infection, whereas 87G7-treated animals were protected from weight loss upon challenge (Fig. 4A). 87G7-treated mice showed reduced lung antigen levels at day 5 after challenge compared with isotype control–treated animals (Fig. 4B). The amount of live virus detected in the lung homogenates decreased by at least one to three orders of magnitude compared with that in mice receiving the control antibody (Fig. 4C). We next assessed the therapeutic activity by 87G7 in the K18-hACE2 mouse model. Intraperitoneal injection of 87G7 (10 mg/kg) at day 1 after nasal challenge with D614G (10^5 PFU) reduced weight loss (13% of

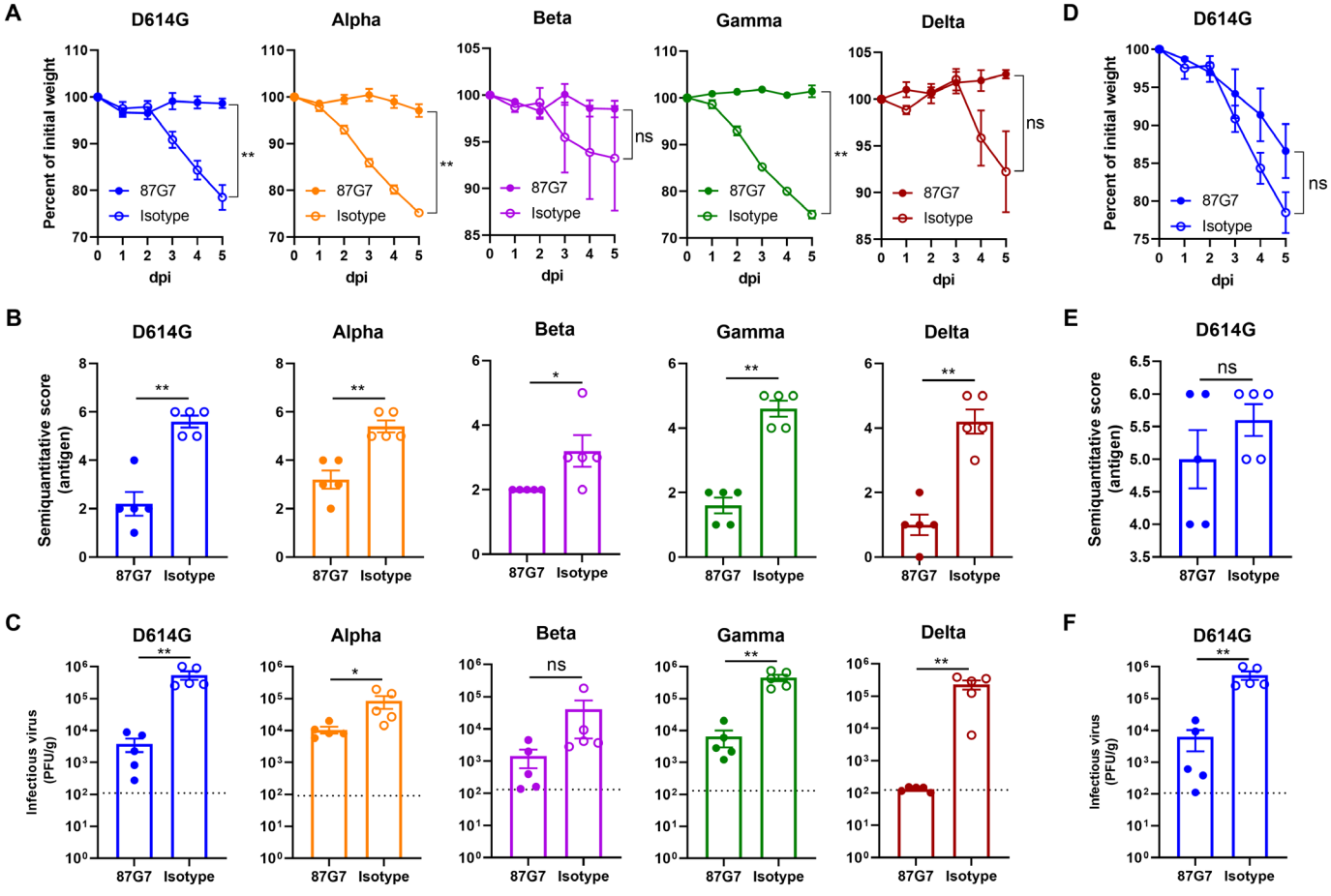

Fig. 4. 87G7 protects mice from challenge with D614G SARS-CoV-2 and Alpha, Beta, Gamma, or Delta variants. Prophylactic and therapeutic treatment was assessed in the K18-hACE2 SARS-CoV-2 mouse model. 87G7 or isotype control mAb was administered intraperitoneally (10 mg/kg of body weight) into groups of mice ($n = 5$) at 24 hours before (**A** to **C**) or after virus challenge (**D** to **F**). Mice were challenged intranasally with 10^5 PFU of SARS-CoV-2 (D614G, Alpha, Beta, Gamma, or Delta) and monitored daily for weight loss (A and D). Five days after challenge, lungs were collected from all mice, and lung viral antigen levels were determined by immunohistochemistry (B and E) (table S2 and fig. S6), and infectious SARS-CoV-2 loads in lung tissue were measured by plaque assay (**C** and **G**). The mean values ± SEM of all data points are shown. Dashed line indicates assay limits of detection. Mann-Whitney *U* test was used to evaluate the statistical difference between the 87G7 and isotype-treated groups (**$P < 0.01$ and *$P < 0.05$; ns, $P > 0.05$). dpi, days postinfection.

their starting weight relative to 22% in the control group), lung antigen levels, and infectious SARS-CoV-2 titers in lungs by two orders of magnitude, relative to IgG1 isotype–treated mice (Fig. 4, D to F). These data highlight the prophylactic and therapeutic efficacy in mice by 87G7 against challenge with SARS-CoV-2 and four VOCs.

We further evaluated the protective efficacy by 87G7 against SARS-CoV-2 variants, including Omicron BA.1 in a hamster model. To assess the prophylactic activity of 87G7, Syrian hamsters were administered intraperitoneally with 87G7 (10 or 20 mg/kg for Omicron-challenged hamsters) or an IgG1 isotype control (10 or 20 mg/kg for Omicron-challenged hamsters), 24 hours before and after intranasal challenge with 10^4 $TCID_{50}$ (median tissue culture infectious dose) of the D614G SARS-CoV-2, Gamma, Delta, or Omicron BA.1 variant. 87G7 administration reduced infectious virus titers in the lungs of most animals in all groups to almost undetectable levels (Fig. 5A). Preventive treatment with 87G7 reduced infectious virus titers in the nasal cavity of the D614G-, Gamma-, Delta-, and Omicron-challenged hamsters by about 1 to 2 logs compared with isotype control antibody–treated groups. Histopathological analysis of lung sections from 87G7-treated hamsters showed a markedly reduced number of lesions for all tested variants compared with those from isotype-treated animals, whereas this pathological

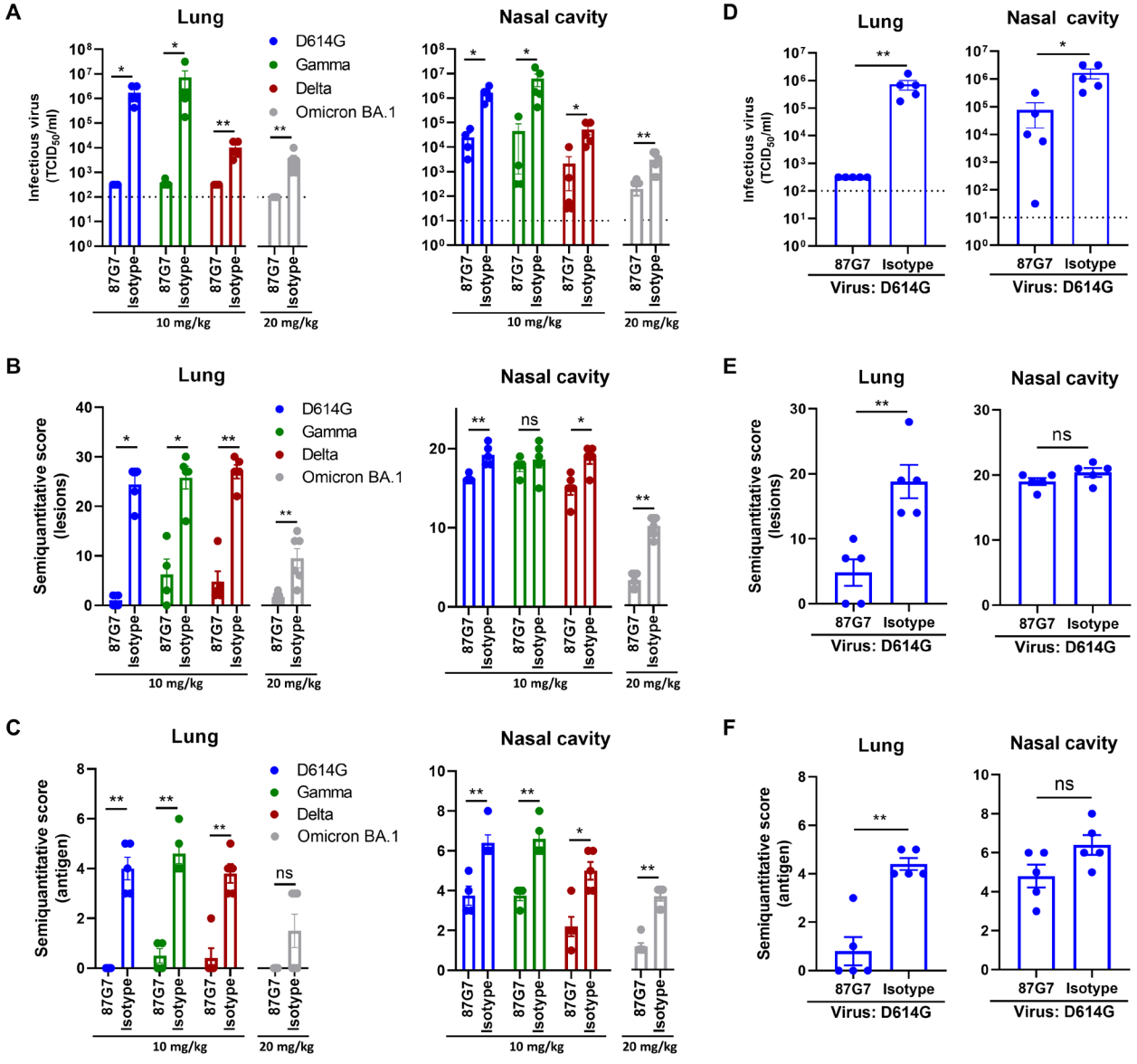

Fig. 5. 87G7 protects hamsters from challenge with D614G SARS-CoV-2 and Gamma, Delta, and Omicron variants. 87G7 or isotype control mAb was administered intraperitoneally (10 mg/kg of body weight or 20 mg/kg for Omicron-challenged hamsters) into groups of Syrian hamsters ($n = 5$ and $n = 6$ for Omicron groups) at 24 hours before (**A** to **C**) or 12 hours after virus challenge (**D** to **F**). Hamsters were challenged intranasally with 10^4 $TCID_{50}$ of D614G SARS-CoV-2, Beta, Gamma, or Omicron. Four days after challenge, hamsters were euthanized, and infectious SARS-CoV-2 titer in lung homogenates and nasal cavity was evaluated by $TCID_{50}$ measurement (A and D). Lung and nasal cavity were examined for lesions by histopathological scoring and the presence of viral antigen by immunohistochemistry (B, C, E, and F) (tables S3 to S5 and figs. S7 to S10). The mean values ± SEM of all data points are shown. Mann-Whitney *U* test was used to evaluate the statistical difference between the 87G7- and isotype-treated groups (**$P < 0.01$ and *$P < 0.05$; ns, $P > 0.05$).

difference in the nasal cavity was less prominent (Fig. 5B). In addition, prophylactic treatment with 87G7 clearly resulted in a notable reduction in antigen expression levels both in the lung and nasal cavity (Fig. 5C). Next, we assessed the therapeutic efficacy of 87G7 in the hamster model. Intraperitoneal injection of 87G7 (10 mg/kg) at 12 hours after intranasal challenge of hamsters with D614G (10^4 $TCID_{50}$) significantly reduced infectious virus titers detected in the lungs (>3 log reduction) and nose (about 1 log reduction) at day 4 after challenge and lowered the number of lesions and antigen levels in these respiratory tissues (Fig. 5, D to F). Overall, the ACE2-blocking 87G7 exhibits broad and potent neutralizing activity and protects against challenge with ancestral SARS-CoV-2 and key VOCs, including Omicron, which is the dominant lineage worldwide.

DISCUSSION

Mutations in Omicron have reshaped the antigenic landscape of the S protein, likely forming a new antigenic cluster relative to all preceding VOCs and VOIs (*15*, *17*, *18*, *20*–*22*). These mutations cause a substantial reduction of neutralizing activity of sera from Pfizer or AstraZeneca vaccine recipients and totally or partially enable neutralization escape by potent neutralizing mAbs including most mAbs that obtained emergency use authorization (*15*, *17*, *18*, *20*, *22*). Typically, the most potent neutralizing antibodies have epitopes that overlap with the ACE2 interaction site and inhibit infection of the prototypic SARS-CoV-2 through ACE2 receptor blockage. However, these antibodies appear notably restricted in binding breadth due to the marked genetic diversity of the ACE2 interaction site among SARS-CoV-2 variants. The 87G7 antibody appeared to be among the few exceptions of ACE2-blocking mAbs that retain potent neutralization against SARS-CoV-2 VOCs including Omicron BA.1 and BA.2 (*5*, *23*). One of these mAbs, LY-CoV1404, binds a conserved epitope on the RBD with partial overlap with the ACE2 binding site, similar to the class III antibody REGN10987 (*23*). In addition, the broadly reactive S2K146 antibody, which targets many of the residues required for ACE2 receptor binding, was also found to retain Omicron neutralization potency (*5*). Although S2K146 has a partially overlapping epitope with 87G7, it appears to make more extensive interactions with the receptor binding site. Further research is needed to compare the neutralizing activity in vivo protection of these broadly neutralizing antibodies, as single mAbs or as combinations, against SARS-CoV-2 and variants.

Whereas effective SARS-CoV-2–specific mAb treatment for hospitalized patients has remained elusive, clinical success has been obtained in the treatment of outpatients with mild or moderate COVID-19 with anti–SARS-CoV-2 mAbs (*35*, *36*). In addition to therapeutic treatment, the development of these mAbs may also be of value for the preventive treatment of seronegative individuals, including those who do not make endogenous antibodies in response to either vaccination or infection (*37*). The antigenic evolution of SARS-CoV-2 has posed a formidable challenge to the development of mAbs for the treatment and prevention of COVID-19. Although neutralization potential has been the first selection criterion of anti–SARS-CoV-2 antibody candidates for clinical use, the antibody potential for cross-neutralization through targeting highly conserved sites on the S protein has now become much more relevant to mitigate the risk of antibody escape by future emerging variants. Our work may contribute to the development of sustainable mAb strategies against COVID-19 using (combinations of) broadly neutralizing antibodies that are more resilient to SARS-CoV-2 antigenic diversity.

MATERIALS AND METHODS

Study design

The aim of the study was to identify SARS-CoV-2 human mAb with potent and broad neutralizing activity against SARS-CoV-2 and VOCs. We immunized H2L2 transgenic mice carrying human VH and VL chain Ig genes with the SARS-CoV-2 S ectodomain and RBD. We generated hybridomas from isolated B cells and used pseudo-virus screening to assess the neutralizing activity of supernatants from hybridomas against pseudo-viruses carrying SARS-CoV-2 S protein with E484K substitution, a residue that is of variance in VOCs with immune escape potential. We used multiple methods including ELISA, BLI, single-particle cryo-EM reconstruction, site-directed mutagenesis, and receptor binding inhibition assays to characterize the antibody binding kinetics and affinity, epitope location, and mechanism of neutralization. Pseudo-virus and live virus assays were used to assess the antibody-mediated neutralization of authentic SARS-CoV-2 and VOCs. We used mouse and hamster infection models to evaluate the antibody-mediated protective efficacy against challenge with SARS-CoV-2 and VOCs. At euthanasia, infectious virus in lung and nasal turbinate tissues was quantified on cultured cells. The pathology in lung and nasal tissues was evaluated using histology and viral antigens by immunohistochemistry.

Viruses and cells

Calu-3 cells were maintained in Opti-MEM I (1X) + GlutaMAX (Gibco) supplemented with 10% fetal bovine serum (FBS), penicillin (100 IU/ml), and streptomycin (100 IU/ml) at 37°C in a humidified CO_2 incubator. Human embryonic kidney (HEK) 293T cells were cultured in Dulbecco's modified Eagle's medium (DMEM) supplemented with 10% FBS, sodium pyruvate (1 mM; Gibco), nonessential amino acids (1×; Lonza), penicillin (100 IU/ml), and streptomycin (100 IU/ml) at 37°C in a humidified CO_2 incubator. Cell lines tested negative for mycoplasma. SARS-CoV-2 isolates were grown to passage 3 on Calu-3 cells. For stock production, infections were performed at a multiplicity of infection of 0.01, and virus was collected at 72 hours after infection, clarified by centrifugation, and stored at −80°C in aliquots. All work with infectious SARS-CoV-2 was performed in a Class II Biosafety Cabinet under BSL-3 conditions at Erasmus Medical Center. Viral genome sequences were determined using Illumina deep sequencing as described before (*38*). The 614G virus (clade B; isolate Bavpat-1; European Virus Archive Global #026 V-03883) passage 3 sequence was identical to the passage 1 (provided by C. Drosten). The Alpha (B.1.1.7; MW947280), Gamma (P.1; OM442897), Delta (B.1.617.2; OM287123), Omicron BA.1 (B.1.1.529.1; OM287553), Omicron BA.2 (B.1.1.529.2), Lambda (C.37), and Mu (B.1.621) variant passage 3 sequences were identical to the original respiratory specimens. For Omicron, the S1 region of the S gene was not covered well because of primer mismatches. Therefore, the S1 region of the original respiratory specimen and passage 3 virus were confirmed to be identical by Sanger sequencing. The Beta variant (B.1.351; OM286905) passage 3 sequence contained two mutations compared with the original respiratory specimen: one synonymous mutation C13860T (Wuhan-Hu-1 position) in ORF1ab and a L71P change in the E gene (T26456C, Wuhan-Hu-1 position). No other minor variants of >40% were detected. SARS-CoV-2 VOCs/VOIs used contained the following S protein changes relative to the Wuhan-Hu-1

strain: Alpha (B.1.1.7), Δ69–70, Δ144, N501Y, A570D, D614G, P681H, T716I, S982A, and D1118H; Beta (B.1.351), L18F, D80A, D215G, Δ241–243, K417N, E484K, N501Y, D614G, and A701V; Gamma (P.1), L18F, T20N, P26S, D138Y, R190S, K417T, E484K, N501Y, D614G, H655Y, T1027I, and V1176F; Delta (B.1.617.2), T19R, G142D, E156G, Δ157–158, L452R, T478K, D614G, P681R, and D950N; Omicron BA.1 (B.1.1.529.1), A67V, Δ69–70, T95I, G142D, Δ143–145, N211I, Δ212, ins214EPE, G339D, S371L, S373P, S375F, K417N, N440K, G446S, S477N, T478K, E484A, Q493R, G496S, Q498R, N501Y, Y505H, T547K, D614G, H655Y, N679K, P681H, N764K, D796Y, N856K, Q954H, N969K, and L981F; Omicron BA.2 (B.1.1.529.2), T19I, L24S, Δ25/27, G142D, V213G, G339D, S371F, S373P, S375F, T376A, D405N, R408S, K417N, N440K, S477N, T478K, E484A, Q493R, Q498R, N501Y, Y505H, D614G, H655Y, N679K, P681H, N764K, D796Y, Q954H, and N969K; Lambda (C.37), G75V, T76I, R246N, Δ247-253, L452Q, F490S, D614G, and T859N; Mu (B.1.621) T95I, Y144S, Y145N, R346K, E484K, N501Y, D614G, P681H, and D950N.

Expression and purification of SARS-CoV-2 S proteins

Human codon-optimized gene was synthesized at GenScript encoding the 6P-stabilized SARS-CoV-2 S ectodomain expression construct (*25*) (S protein residues 1 to 1213, Wuhan-Hu-1 strain: GenBank: QHD43416.1) with a C-terminal T4 foldon trimerization motif, followed by an octa-histidine tag and a Twin-Strep-tag (*39*). Constructs encoding S1 (residues 1 to 682), the NTD (residues 1 to 294), or RBD (residues 329 to 538) of SARS-CoV-2 S (Wuhan-Hu-1 strain), C-terminally tagged with Strep-tag, have been described before (*40*). Human codon-optimized genes were synthesized encoding S1 proteins of Alpha (B.1.1.7), Beta (B.1.351), Gamma (P.1), Delta (B.1.617.2), and Omicron (B.1.1.529) VOCs described above, including a C-terminal Strep-tag. All proteins were expressed transiently in HEK-293T [American Type Culture Collection (ATCC), CRL-11268] cells from pCAGGS expression plasmids, and secreted proteins were purified from culture supernatants using streptactin beads (IBA) following the manufacturer's protocol. S variants with single-site residue substitutions were generated using Q5 High-fidelity DNA polymerase (NEB)–based site-directed mutagenesis.

Immunization, hybridoma culturing, and production of (recombinant) mAbs

Harbour H2L2 mice (Harbour BioMed) were immunized using heterologous DNA/protein immunization protocol 16-512-22 under animal license (AVD101002016512) approved by CCD (Dutch Central Comity for animal experimentation). Mice were housed in a specific pathogen–free facility with cage enrichment, light switched on at 0700 and switched off at 1900 and with humidity at around 40%. Both female and male H2L2 mice were used. The female mice were housed up to four per individually ventilated cage (IVC), whereas males were in separate IVC cages to prevent fighting. Food was standard and water and food intake ad libitum. Mice were immunized intradermally three times biweekly with 50 μg of plasmid DNA encoding the Wuhan-Hu-1 SARS-CoV-2 S ectodomain trimer in 20 μl of water, using the AgilePulse Intradermal electroporator system (BTX) according to the manufacturer's instructions. After priming with DNA, immunization was continued in biweekly intervals by subcutaneous and/or intraperitoneal injection of 20 to 30 μg of antigen preparations formulated with Ribi Adjuvant System (Sigma-Aldrich) according to the manufacturer's instructions, alternating between the S ectodomain trimer and RBD of Wuhan-Hu-1 SARS-CoV-2 as antigens. Antigen-specific antibody titers were monitored during immunization by taking blood samples from the mice and performing antigen-specific ELISA. High-titer mice were euthanized 3 to 5 days after the last protein boost (six in total), and lymphoid organs (spleen and lymph nodes) were dissected. Single-cell suspensions were generated by gently pressing and moving the lymphoid tissue in the presence of RPMI 1640 medium with a 2-ml syringe rubber part plunger against the 40-μm nylon cell strainer (Falcon) fitted in a 50-ml conical tube. Single cells were then fused to generate hybridomas by polyethylene glycol (PEG)–mediated fusion with Sp2/0 myeloma cells (ATCC, #CRL-1581). Briefly, separate fusions were done for each mouse (spleen and lymph node cells), and cells were washed in Fusion medium (RPMI 1640) and transferred to the new 50-ml tube. Sp2/0 cells were cultured in advance [RPMI 1640, 10% FBS, L-glutamine, penicillin (100 IU/ml), streptomycin (100 IU/ml), and 0.4% Hybridoma Fusion and Cloning Supplement (HFCS)]. For each fusion, we used 1.0×10^8 Sp2/0 cells. Sp2/0 cells were washed in Fusion medium and added to the tube with single-cell suspension of splenocytes/lymphocytes from one mouse (~2.0×10^8 to 2.5×10^8 cells). Fusion medium was added to the 50-ml mark. After centrifugation (5 min at 400*g*), supernatant was discarded, and pellet was disrupted by gently tapping the bottom of the tube. Tube was placed at 37°C, and 1 ml of prewarmed PEG (PEG 1500, Roche) was slowly added over a period of 1 min to the cell pellet by dripping down the side of the tube under gentle stirring. After additional incubation for 1.5 min, 2 ml of prewarmed Fusion medium was added to the tube over a period of 2 min under gentle stirring. An additional 14 ml of Fusion medium was added to the tube over a period of 2 min under gentle stirring, and the tube was left for 10 min at 37°C. Cells were spun down, resuspended in 300 ml of selection medium [advanced RPMI 1640, GlutaMAX, 2% HFCS, 0.4 μM aminopterin, 100 μM hypoxanthine, 16 μM thymidine, 10% FBS, penicillin (100 IU/ml), and streptomycin (100 IU/ml)], and plated in 96-well plates (200 μl per well). On days 6 and 7, we added 100 μl of post-fusion selection medium to each well. Screening of hybridoma supernatants was started 10 to 14 days after fusion. Supernatants from 96-well plates (estimated to have one to four hybridoma clones per well) were screened for SARS-CoV-2 S binding antibodies by ELISA using SARS-CoV-2 S ectodomain–coated plates (see below) and for neutralizing antibodies using the SARS-CoV-2 pseudo-virus neutralization assay (see below). Selected hybridomas were subcloned by limited dilution and retested in ELISA and pseudo-virus assay.

Production of recombinant human antibodies using HEK-293T was described previously (*41*). Briefly, gene blocks encoding the VH and VL chain sequences of 87G7 and of benchmark mAbs REGN10933, REGN10987 [Protein Data Bank (PDB) ID: 6XDG] (*42*), S309 (PDB ID: 6WPS) (*43*), CR3022 (GenBank accession numbers: DQ168569.1 and DQ168570.1) (*44*), and 47D11 (GenBank accession numbers: MW881223.1 and MW881224.1) (*40*) were synthesized. VH and VL sequences were separately cloned into the expression plasmids with human IgG1 HC and human kappa chain constant regions, respectively, using the HBM vectors pHBM 000254 (VH into pTT5-mIGK-hIgG1_HCv2) and HBM 000265 (VK into pTT5mIgK-hIgG_KCv2). Recombinant human antibodies were expressed in HEK-293T cells after transient transfection using polyethylenimine with pairs of the IgG1 HC and LC expression plasmids. At 18 hours after transfection, the transfection mixture was replaced by 293 SFM II expression medium (Invitrogen), supplemented with sodium bicarbonate (3.7 g/liter), glucose (2.0 g/liter), Primatone RL-UF

(3.0 g/liter), penicillin (100 IU/ml), streptomycin (100 IU/ml), GlutaMAX, and 1.5% dimethyl sulfoxide. Tissue culture supernatants were harvested 5 to 6 days after transfection, and recombinant antibodies were purified using Protein A Sepharose (IBA) according to the manufacturer's instructions.

ELISA analysis of antibody binding to SARS-CoV-2 S antigens

Purified S antigens (1 μg/ml) were coated onto 96-well NUNC Maxisorp plates (Thermo Fisher Scientific) at room temperature (RT) for 3 hours, followed by three washing steps with phosphate-buffered saline (PBS) containing 0.05% Tween 20. Plates were blocked with 3% bovine serum albumin (BSA; Fitzgerald) in PBS with 0.1% Tween 20 at 4°C overnight. Antibodies in hybridoma supernatants diluted in PBS containing 3% BSA and 0.1% Tween 20 were allowed to bind to the ELISA plates at RT for 1 hour, and binding was determined using a 1:3000 diluted horseradish peroxidase (HRP)–conjugated mouse anti-rat IgG1, IgG2b, and IgG2 mix (Absea) for 1 hour at RT. Alternatively, 87G7 mAb was allowed to bind to the plates at fivefold serial dilutions, starting at 10 μg/ml diluted in PBS containing 3% BSA and 0.1% Tween 20, at RT for 1 hour. Antibody binding to the S proteins was determined using a 1:2000 diluted HRP-conjugated goat anti-human IgG (ITK Southern Biotech) for 1 hour at RT. HRP activity was measured at 450 nm using tetramethylbenzidine substrate (BioFX) and an ELISA plate reader (EL-808, BioTek).

Antibody binding kinetics and affinity measurement

87G7 (21 nM) was loaded onto Protein A biosensors (ForteBio) for 10 min. Antigen binding was performed by incubating the biosensor with twofold dilutions of recombinant SARS-CoV-2 S1 monomer or S ectodomain trimer for 10 min, followed by a long dissociation step (30 min) to observe the decrease in the binding response. The affinity constant K_D was calculated using 1:1 Langmuir binding model on Fortebio Data Analysis 7.0 software.

BLI-based binding competition assay

Binding competition was performed using BLI (Octet Red348, ForteBio), as described previously (*40*, *41*). Briefly, SARS-CoV-2 S ectodomain trimer (50 μg/ml) was immobilized onto the anti-strep mAb-coated protein A biosensor. After a brief washing step, the biosensor tips were immersed into a well containing primary mAb (50 μg/ml) for 15 min and subsequently into a well for 15 min containing the competing mAb (secondary mAb; 50 μg/ml) or recombinant soluble ACE2. A 3- to 5-min washing step in PBS was included in between the steps.

ELISA-based receptor binding inhibition assay

The ACE2 receptor binding inhibition assay was performed as described previously (*40*, *41*). Recombinant soluble ACE2 was coated on NUNC Maxisorp plates (Thermo Fisher Scientific) at 1 μg per well at RT for 3 hours. Plates were washed three times with PBS containing 0.05% Tween 20 and blocked with 3% BSA (Fitzgerald) in PBS containing 0.1% Tween 20 at 4°C overnight. Recombinant SARS-CoV-2 S RBD domain (200 nM) and serially diluted mAbs were mixed and incubated for 2 hours at RT. The mixture was added to the plate for 2 hours at 4°C, after which the plates were washed three times. Binding of SARS-CoV-2 S RBD domain to ACE2 was detected using 1:2000 diluted HRP-conjugated anti-StrepMAb (IBA) that recognizes the Strep-tag affinity tag on the SARS-CoV-2 S RBD domain. Detection of HRP activity was performed as described above (ELISA section).

Pseudo-virus neutralization assay

Human codon-optimized genes encoding the S proteins of SARS-CoV-2 S proteins corresponding to ancestral Wuhan-Hu-1 virus (GenBank: NC_045512.2) or VOCs Alpha (B.1.1.7), Beta (B.1.351), Gamma (P.1), Delta (B.1.617.2), and Omicron (B.1.1.529) were synthesized by GenScript. The production of SARS-CoV-2 S pseudo-typed VSV and the neutralization assay were performed as described previously (*40*). Briefly, HEK-293T cells at 70 to 80% confluency were transfected with the pCAGGS expression vectors encoding SARS-CoV-2 S with a C-terminal cytoplasmic tail 18-residue truncation to increase cell surface expression levels. Cells were infected with VSV G–pseudo-typed VSVΔG bearing the firefly (*Photinus pyralis*) luciferase reporter gene at 48 hours after transfection. Twenty-four hours later, the supernatant was harvested and filtered through a 0.45-μm membrane. Pseudo-typed VSV was titrated on VeroE6 cells. In the virus neutralization assay, threefold serially diluted mAbs were preincubated with an equal volume of virus at RT for 1 hour, then inoculated on VeroE6 cells, and further incubated at 37°C. Alternatively, pseudo-virus was preincubated with 1/10 volume of H2L2 hybridoma culture supernatant for 1 hour, before infection of Vero cells. After 20 hours, cells were washed once with PBS and lysed with Passive lysis buffer (Promega). The expression of firefly luciferase was measured on a Berthold Centro LB 960 plate luminometer using D-luciferin as a substrate (Promega). The percentage of neutralization was calculated as the ratio of the reduction in luciferase readout in the presence of mAbs normalized to luciferase readout in the absence of mAb. The IC_{50} values were determined using four-parameter logistic regression (GraphPad Prism v8.3.0).

Live virus neutralization assay

Human mAbs were tested for live virus neutralization using a plaque reduction neutralization (PRNT) assay. PRNT was performed according to a previously published protocol (*38*), with minor modifications. Briefly, 50 μl of serially diluted antibody in Opti-MEM I (IX) + GlutaMAX (Gibco, USA) was mixed 1:1 with virus (400 PFU) and incubated at 37°C for 1 hour before layering over fully confluent monolayers of Calu-3 cells [washed once prior with Opti-MEM I (IX) + GlutaMAX]. After 8 hours of infection, the cells were fixed with formalin, permeabilized with 70% ethanol, washed in PBS, and stained using rabbit anti–SARS-CoV nucleocapsid (1:2000 in 0.1% BSA in PBS; SinoBiological), followed by goat anti-rabbit Alexa Fluor 488 antibody (1:2000 in 0.1% BSA in PBS; Invitrogen). Plates were scanned on the Amersham Typhoon Biomolecular Imager (GE Healthcare, USA). Data were analyzed using ImageQuantTL 8.2 image analysis software (GE Healthcare). The PRNT titer was calculated using GraphPad Prism 9, calculating a 50% reduction in infected cell counts based on nonlinear regression with bottom constraints of 0% and top constraints of 100%.

Cryo-EM sample preparation and data collection

The 87G7 Fab fragment was digested from the IgG with papain using a Pierce Fab Preparation Kit (Thermo Fisher Scientific), according to the manufacturer's instructions. S-Fab complexes were prepared under two conditions. For the first condition, 4 μl of SARS-CoV-2 hexaproline S ectodomain, at a concentration of 28 μM (based on the molecular weight of the S protomer) was combined with 1 μl of 150 μM 87G7 Fab and incubated for ~10 min at RT before blotting and plunge freezing. For the second condition, 3.5 μl of 28 μM SARS-CoV-2 hexaproline S ectodomain was combined with 1 μl of 150 μM 87G7 Fab and then incubated for ~10 min at RT. Immediately before blotting and plunge freezing, 0.5 μl of 0.2% (w/v) fluorinated octyl maltoside (FOM) was added to the sample, resulting in a final FOM concentration of 0.02% (w/v). For both conditions,

3 μl of S-Fab complex was applied to glow-discharged (20 mA, 30 s; Quorum GloQube) Quantifoil R1.2/1.3 grids (Quantifoil Micro Tools GmbH), blotted for 5 s using blot force 2 and plunge-frozen into liquid ethane using Vitrobot Mark IV (Thermo Fisher Scientific). The data were collected on the Thermo Fisher Scientific Krios G4 Cryo Transmission Electron Microscope equipped with Selectris X Imaging Filter (Thermo Fisher Scientific) and Falcon 4 Direct Electron Detector (Thermo Fisher Scientific) operated in Electron-Event representation mode. Data processing was performed in Relion 3.1 (*45*) and cryoSPARC (*46*) single-particle analysis suites. Raw data were imported in cryoSPARC. After Patch motion correction and Patch CTF estimation, 313,636 particles were picked from 1331 images from 0.02% FOM dataset, and 621,175 particles were picked from 2500 images without FOM. After 2D classification and heterogeneous refinement, the best particle stack consisting of 133,550 particles was subjected to nonuniform refinement (*47*) with C3 symmetry imposed, yielding a S-Fab complex cryo-EM map with an overall resolution of 2.9 Å. After global refinement, a soft mask encompassing one RBD with the Fab bound was made in UCSF Chimera (*48*). Particles were imported into Relion 3.1, and, using the "relion_particle_symmetry_expand" tool, each particle from the C3 symmetry–imposed reconstruction was assigned three orientations corresponding to its symmetry-related views. The soft mask was placed over a single RBD-Fab region of the map, and the symmetry-expanded particles were subjected to masked 3D classification without alignment using a regularization parameter ("T" number) of 20. After a single round of focused classification, the best particle stack consisting of 72,118 particles was imported back to cryoSPARC and refined without imposing symmetry using the local refinement job, yielding a map with a global resolution of 4.9 Å. The nominal resolutions and local resolution estimations for the global and local refinements were performed in Relion 3.1. The "Gold Standard" Fourier shell correlation (FSC) criterion (FSC = 0.143) was used for resolution estimates. Last, the globally and locally refined maps were masked and sharpened using DeepEMhancer tool (*49*), as implemented in COSMIC2 (*50*), and combined using the "vop add" command in UCSF Chimera (*48*). Data collection and reconstruction parameters can be found in table S1.

Model building and refinement

UCSF Chimera (*48*) (version 1.15.0) and Coot (*51*) (version 0.9.6) were used for model building. As a starting point for modeling the 87G7-bound S, the crystal structure of the SARS-CoV-2-S NTD [residues 14 to 308; PDB ID: 7B62 (*52*)], the fully open SARS-CoV-2-S model [residues 309 to 332 and 527 to 1145; PDB ID: 7K4N (*28*)], and RBD crystal structure [residues 333 to 526; PDB ID 6M0J (*53*)] were individually rigid-body fitted into the composite density map using the UCSF Chimera "Fit in map" tool (*48*). Subsequently, the models were combined, and the peptide sequence was adjusted to match the 6P S construct used in this study. For modeling the 87G7 Fab fragment, atomic coordinates of the HC and the LC variable regions were generated using the phyre2 server (*54*) and rigid-body fitted into the EM density map using the UCSF Chimera fit in map tool and then combined with the spike model. The resulting model was then edited in Coot using the "real-space refinement" (*51*), carbohydrate module (*55*), and "sphere refinement" tool. Iterative rounds of manual fitting in Coot and real space refinement in Phenix (*56*) were carried out to improve nonideal rotamers, bond angles, and Ramachandran outliers. During refinement with Phenix, secondary structure and noncrystallographic symmetry restraints were imposed. The final model was validated with MolProbity (*57*), EMRinger (*58*), and Privateer (glycans) (*59*, *60*).

Analysis and visualization

S residues interacting with 87G7 were identified using PDBePISA (*61*) and LigPlot^{+} (*62*). Surface coloring of the SARS-CoV-2 RBD according to sequence conservation and the Kyte-Doolittle hydrophobicity scale was performed in UCSF ChimeraX (*63*). The UCSF Chimera "MatchMaker" tool was used to obtain root mean square deviation values, using default settings. Figures were generated using UCSF Chimera (*48*) and UCSF ChimeraX (*63*). Structural biology applications used in this project were compiled and configured by SBGrid (*64*).

Mouse challenge experiment

In vivo prophylactic and therapeutic efficacy of mAb 87G7 against challenge with SARS-CoV-2 and four VOCs was evaluated in heterozygous K18-hACE2 C57BL/6J mice [strain: 2B6.Cg-Tg(K18-ACE2)2Prlmn/J] obtained from the Jackson Laboratory. Groups of 14-week-old female mice (n = 5), were given 200 μg of 87G7 or isotype control antibody (equivalent to 10 mg of the antibody per kilogram) by intraperitoneal injection, 16 hours before or 1 day after intranasal inoculation with a lethal dose of the indicated SARS-CoV-2 strain (10^5 PFU per mouse). Virus inoculations were performed under anesthesia that was induced with isoflurane, and all efforts were made to minimize animal suffering. All animals were housed in a self-contained ventilated rack (Tecniplast, IT), with the light switched on at 0730 and switched off at 1930. The ambient temperature was 19.5° to 22°C and with humidity at 35 to 40%. Animal protection studies were carried out under the animal permit PROEX-146.6/20, approved by the Community of Madrid (Spain), and performed in biosafety level 3 facilities at CISA-INIA (Madrid).

To quantify infectious SARS-CoV-2 virus particles, one-fourth of the right lung was homogenized using a MACS homogenizer (Miltenyi Biotec) according to the manufacturer's protocols. Virus titrations were done using plaque assay performed on Vero E6 cells following standard procedures. Briefly, cells were overlaid with DMEM containing 0.6% low-melting agarose and 2% FBS, fixed with 10% formaldehyde, and stained with 0.1% crystal violet at 72 hours after infection.

To quantify viral antigen by immunohistochemistry, left lung lobes were fixed in 10% buffered formalin (Chemie Vertrieb GmbH & Co Hannover KG, Hannover, Germany). Left lung lobes were prefixed by injections of 10% buffered formalin as recommended by Meyerholz *et al.* (*65*) to ensure an optimal histopathological evaluation (table S2).

Hamster challenge experiment

During the experiment, the animals were under veterinary observation, and all efforts were made to minimize distress. Approval for the experiments was given by the German Niedersächsisches Landesamt für Verbraucherschutz und Lebensmittelsicherheit (LAVES file number 21/3755) and by the Dutch authorities (project license number 27700202114492-WP12). Syrian hamsters (*Mesocricetus auratus*, 6 to 10 weeks old, Janvier Labs) were housed under BSL-3 conditions, starting 10 days before the experiment. 87G7 or a non–SARS-CoV-2 human IgG control antibody was injected intraperitoneally in a volume of 500 μl. The hamsters were challenged intranasally, 24 hours after or 12 hours before antibody inoculation, with 10^4 $TCID_{50}$ of the respective SARS-CoV-2 variants, respectively. The animals were monitored for body weight loss and clinical symptoms twice daily until they were humanely euthanized 4 days

after infection. Antibody injection with challenge virus and euthanasia were performed under isoflurane anesthesia. Left nasal turbinates and left lung lobe were fixed in 10% buffered formalin (Chemie Vertrieb GmbH & Co Hannover KG, Hannover, Germany) from the investigated hamsters. Left lung lobes were prefixed by injections of 10% buffered formalin (*65*) to ensure an optimal histopathological evaluation. Left nasal turbinates, after formalin fixation, were decalcified in soft tissue decalcifier (Roth, #6484.2) for about 14 days before routine tissue processing.

To quantify infectious SARS-CoV-2 virus particles, lung and nasal turbinate tissues were homogenized using a TissueLyser II (QIAGEN), and infectious SARS-CoV-2 virus particles in tissue homogenates were quantified on Vero E6 cells. Cells were infected with 10-fold serial dilutions of the homogenized tissue prepared in DMEM + 2% FBS (starting dilution 100- and 10-fold for lung and nasal turbinate homogenate, respectively). Plates were further incubated in a humidified atmosphere, at 37°C and 5% CO_2. Cytopathic effect was evaluated 5 days after infection. Omicron samples were titrated in Calu-3 cells because of the low infectivity of Omicron in Vero cells. In this case, after 5 days of incubation, cells were fixed with 4% paraformaldehyde (PFA) and stained using an anti–SARS-CoV-2 nucleocapsid antibody (SinoBiological). Virus titers ($TCID_{50}$ per milliliter) were calculated using the Spearman-Karber method.

Formalin-fixed, paraffin-embedded (FFPE) tissue was used for histology and immunohistochemistry. Histopathological lesions were evaluated on hematoxylin-eosin–stained sections. For the detection of viral antigen in Syrian golden hamsters, immunohistochemistry with an mAb detecting SARS-CoV/SARS-CoV-2 nucleocapsid (SinoBiological, 40143-MM05) was performed on FFPE tissue sections, as described previously (*66*, *67*). Briefly, tissue sections were dewaxed and rehydrated, followed by endogenous peroxidase blocking for 30 min at RT. Antigen retrieval was performed in Na_2H_2EDTA buffer for 20 min in a microwave at 800 W. The primary antibody (dilution, 1:4000) was applied for 1 hour at RT. Sections were subsequently rinsed, and secondary labeling was performed using the respective peroxidase-labeled polymer (Dako Agilent Pathology Solutions, K4003) for 30 min at RT. Visualization of the reaction was accomplished by incubation in chromogen 3,3-diaminobenzidine tetrahydrochloride (0.05%) and 0.03% H_2O_2 in PBS for 5 min. The slides were afterward counterstained with Mayer's hematoxylin for 1 min. Nasal turbinates were evaluated on a full-length longitudinal section of the nose including respiratory and olfactory epithelium. Assessment of histopathological lesions in the nasal turbinates was performed with a semiquantitative score system, as described previously with minor modifications. Quantification of the viral antigen in the nasal epithelium was performed using a semiquantitative score. The left lung lobes of the hamsters were evaluated on one cross section (at the level of the entry of the main bronchus) and one longitudinal section (along the main bronchus) of the entire left lung lobe. Assessment of histopathological lesions and viral load in the lung was performed with a semiquantitative scoring system, as described previously with minor modifications (*68*). System for semiquantitative scoring of histopathological lesions and viral antigen in nose and lung is shown in tables S3 to S5. Histopathological semiquantitative evaluations were performed by veterinary pathologists (G.B., M.C., and F.A.) and subsequently confirmed by a European board-certified veterinary pathologist (W.B.). During the evaluation, the pathologist was blinded regarding the treatment groups and used virus strains.

Statistics

The difference between two independent groups was measured using a two-tailed nonparametric Mann-Whitney *U* test. A *P* value of less than 0.05 was considered significant. $*P < 0.05$, $**P < 0.01$, $***P < 0.001$, and $****P < 0.0001$; ns (not significant), $P \geq 0.05$. GraphPad Prism version 9.3.1 (GraphPad Software) was used to perform data analysis and statistics.

SUPPLEMENTARY MATERIALS

www.science.org/doi/10.1126/sciimmunol.abp9312
Figs. S1 to S10
Tables S1 to S6

View/request a protocol for this paper from *Bio-protocol*.

REFERENCES AND NOTES

1. K. Tao, P. L. Tzou, J. Nouhin, R. K. Gupta, T. de Oliveira, S. L. Kosakovsky Pond, D. Fera, R. W. Shafer, The biological and clinical significance of emerging SARS-CoV-2 variants. *Nat. Rev. Genet.* **22**, 757–773 (2021).
2. P. Wang, R. G. Casner, M. S. Nair, M. Wang, J. Yu, G. Cerutti, L. Liu, P. D. Kwong, Y. Huang, L. Shapiro, D. D. Ho, Increased resistance of SARS-CoV-2 variant P.1 to antibody neutralization. *Cell Host Microbe* **29**, 747–751.e4 (2021).
3. P. Wang, M. S. Nair, L. Liu, S. Iketani, Y. Luo, Y. Guo, M. Wang, J. Yu, B. Zhang, P. D. Kwong, B. S. Graham, J. R. Mascola, J. Y. Chang, M. T. Yin, M. Sobieszczyk, C. A. Kyratsous, L. Shapiro, Z. Sheng, Y. Huang, D. D. Ho, Antibody resistance of SARS-CoV-2 variants B.1.351 and B.1.1.7. *Nature* **593**, 130–135 (2021).
4. A. Wilhelm, M. Widera, K. Grikscheit, T. Toptan, B. Schenk, C. Pallas, M. Metzler, N. Kohmer, S. Hoehl, F. A. Helfritz, T. Wolf, U. Goetsch, S. Ciesek, Reduced neutralization of SARS-CoV-2 Omicron variant by vaccine sera and monoclonal antibodies. medRxiv 2021.12.07.21267432 [Preprint]. 8 December 2021. https://doi.org/10.1101/2021.12.07.21267432.
5. E. Cameroni, J. E. Bowen, L. E. Rosen, C. Saliba, S. K. Zepeda, K. Culap, D. Pinto, L. A. Van Blargan, A. De Marco, J. di Iulio, F. Zatta, H. Kaiser, J. Noack, N. Farhat, N. Czudnochowski, C. Havenar-Daughton, K. R. Sprouse, J. R. Dillen, A. E. Powell, A. Chen, C. Maher, L. Yin, D. Sun, L. Soriaga, J. Bassi, C. Silacci-Fregni, C. Gustafsson, N. M. Franko, J. Logue, N. T. Iqbal, I. Mazzitelli, J. Geffner, R. Grifantini, H. Chu, A. Gori, A. Riva, O. Giannini, A. Ceschi, P. Ferrari, P. E. Cippà, A. Franzetti-Pellanda, C. Garzoni, P. J. Halfmann, Y. Kawaoka, C. Hebner, L. A. Purcell, L. Piccoli, M. S. Pizzuto, A. C. Walls, M. S. Diamond, A. Telenti, H. W. Virgin, A. Lanzavecchia, G. Snell, D. Veesler, D. Corti, Broadly neutralizing antibodies overcome SARS-CoV-2 Omicron antigenic shift. *Nature* **602**, 664–670 (2022).
6. S. Cele, L. Jackson, D. S. Khoury, K. Khan, T. Moyo-Gwete, H. Tegally, J. E. San, D. Cromer, C. Scheepers, D. Amoako, F. Karim, M. Bernstein, G. Lustig, D. Archary, M. Smith, Y. Ganga, Z. Jule, K. Reedoy, S.-H. Hwa, J. Giandhari, J. M. Blackburn, B. I. Gosnell, S. S. A. Karim, W. Hanekom; NGS-SA; COMMIT-KZN Team, A. von Gottberg, J. Bhiman, R. J. Lessells, M.-Y. S. Moosa, M. P. Davenport, T. de Oliveira, P. L. Moore, A. Sigal, SARS-CoV-2 Omicron has extensive but incomplete escape of Pfizer BNT162b2 elicited neutralization and requires ACE2 for infection. *Nature* 2021.12.08.21267417 (2021).
7. W. Dejnirattisai, R. H. Shaw, P. Supasa, C. Liu, A. S. Stuart, A. J. Pollard, X. Liu, T. Lambe, D. Crook, D. I. Stuart, J. Mongkolsapaya, J. S. Nguyen-Van-Tam, M. D. Snape, G. R. Screaton; Com-COV2 study group, Reduced neutralisation of SARS-CoV-2 omicron B.1.1.529 variant by post-immunisation serum. *Lancet* **399**, 234–236 (2022).
8. T. G. Caniels, I. Bontjer, K. van der Straten, M. Poniman, J. A. Burger, B. Appelman, A. H. A. Lavell, M. Oomen, G.-J. Godeke, C. Valle, R. Mögling, H. D. G. van Willigen, E. Wynberg, M. Schinkel, L. A. van Vught, D. Guerra, J. L. Snitselaar, D. N. Chaturbhuj, I. C. Martin, Amsterdam UMC COVID-19 S3/HCW study group, J. P. Moore, M. D. de Jong, C. Reusken, J. J. Sikkens, M. K. Bomers, G. J. de Bree, M. J. van Gils, D. Eggink, R. W. Sanders, Emerging SARS-CoV-2 variants of concern evade humoral immune responses from infection and vaccination. *Sci. Adv.* **7**, eabj5365 (2021).
9. W. F. Garcia-Beltran, K. J. S. Denis, A. Hoelzemer, E. C. Lam, A. D. Nitido, M. L. Sheehan, C. Berrios, O. Ofoman, C. C. Chang, B. M. Hauser, J. Feldman, A. L. Roederer, D. J. Gregory, M. C. Poznansky, A. G. Schmidt, A. J. Iafrate, V. Naranbhai, A. B. Balazs, mRNA-based COVID-19 vaccine boosters induce neutralizing immunity against SARS-CoV-2 Omicron variant. *Cell* **185**, 457–466.e4 (2022).
10. M. J. van Gils, A. H. A. Lavell, K. van der Straten, B. Appelman, I. Bontjer, M. Poniman, J. A. Burger, M. Oomen, J. H. Bouhuijs, L. A. van Vught, M. A. Slim, M. Schinkel, E. Wynberg, H. D. G. van Willigen, M. Grobben, K. Tejjani, J. Snitselaar, T. G. Caniels; Amsterdam UMC COVID-19 S3/HCW study group, A. P. J. Vlaar, M. Prins, M. D. de Jong, G. J. de Bree, J. J. Sikkens, M. K. Bomers, R. W. Sanders, Four SARS-CoV-2 vaccines induce quantitatively

different antibody responses against SARS-CoV-2 variants. medRxiv 2021.09.27.21264163 [Preprint]. 28 September 2022. https://doi.org/10.1101/2021.09.27.21264163.

11. M. Hoffmann, N. Krüger, S. Schulz, A. Cossmann, C. Rocha, A. Kempf, I. Nehlmeier, L. Graichen, A.-S. Moldenhauer, M. S. Winkler, M. Lier, A. Dopfer-Jablonka, H.-M. Jäck, G. M. N. Behrens, S. Pöhlmann, The Omicron variant is highly resistant against antibody-mediated neutralization: Implications for control of the COVID-19 pandemic. *Cell* **185**, 447–456.e11 (2022).
12. C. O. Barnes, C. A. Jette, M. E. Abernathy, K.-M. A. Dam, S. R. Esswein, H. B. Gristick, A. G. Malyutin, N. G. Sharaf, K. E. Huey-Tubman, Y. E. Lee, D. F. Robbiani, M. C. Nussenzweig, A. P. West Jr., P. J. Bjorkman, SARS-CoV-2 neutralizing antibody structures inform therapeutic strategies. *Nature* **588**, 682–687 (2020).
13. A. J. Greaney, A. N. Loes, L. E. Gentles, K. H. D. Crawford, T. N. Starr, K. D. Malone, H. Y. Chu, J. D. Bloom, Antibodies elicited by mRNA-1273 vaccination bind more broadly to the receptor binding domain than do those from SARS-CoV-2 infection. *Sci. Transl. Med.* **13**, eabi9915 (2021).
14. A. J. Greaney, T. N. Starr, C. O. Barnes, Y. Weisblum, F. Schmidt, M. Caskey, C. Gaebler, A. Cho, M. Agudelo, S. Finkin, Z. Wang, D. Poston, F. Muecksch, T. Hatziioannou, P. D. Bieniasz, D. F. Robbiani, M. C. Nussenzweig, P. J. Bjorkman, J. D. Bloom, Mapping mutations to the SARS-CoV-2 RBD that escape binding by different classes of antibodies. *Nat. Commun.* **12**, 4196 (2021).
15. L. Liu, S. Iketani, Y. Guo, J. F.-W. Chan, M. Wang, L. Liu, Y. Luo, H. Chu, Y. Huang, M. S. Nair, J. Yu, K. K.-H. Chik, T. T.-T. Yuen, C. Yoon, K. K.-W. To, H. Chen, M. T. Yin, M. E. Sobieszczyk, Y. Huang, H. H. Wang, Z. Sheng, K.-Y. Yuen, D. D. Ho, Striking antibody evasion manifested by the Omicron variant of SARS-CoV-2. *Nature* **602**, 676–681 (2021).
16. M. McCallum, N. Czudnochowski, L. E. Rosen, S. K. Zepeda, J. E. Bowen, A. C. Walls, K. Hauser, A. Joshi, C. Stewart, J. R. Dillen, A. E. Powell, T. I. Croll, J. Nix, H. W. Virgin, D. Corti, G. Snell, D. Veesler, Structural basis of SARS-CoV-2 Omicron immune evasion and receptor engagement. *Science* **375**, 864–868 (2022).
17. Y. Cao, J. Wang, F. Jian, T. Xiao, W. Song, A. Yisimayi, W. Huang, Q. Li, P. Wang, R. An, J. Wang, Y. Wang, X. Niu, S. Yang, H. Liang, H. Sun, T. Li, Y. Yu, Q. Cui, S. Liu, X. Yang, S. Du, Z. Zhang, X. Hao, F. Shao, R. Jin, X. Wang, J. Xiao, Y. Wang, X. S. Xie, Omicron escapes the majority of existing SARS-CoV-2 neutralizing antibodies. *Nature* **602**, 657–663 (2022).
18. D. Planas, N. Saunders, P. Maes, F. Guivel-Benhassine, C. Planchais, J. Buchrieser, W.-H. Bolland, F. Porrot, I. Staropoli, F. Lemoine, H. Péré, D. Veyer, J. Puech, J. Rodary, G. Baela, S. Dellicour, J. Raymenants, S. Gorissen, C. Geenen, B. Vanmechelen, T. Wawina-Bokalanga, J. Martí-Carrerasi, L. Cuypers, A. Sève, L. Hocqueloux, T. Prazuck, F. A. Rey, E. Simon-Lorrière, T. Bruel, H. Mouquet, E. André, O. Schwartz, Considerable escape of SARS-CoV-2 Omicron to antibody neutralization. *Nature* **602**, 671–675 (2021).
19. A. Aggarwal, A. O. Stella, G. Walker, A. Akerman, V. Milogiannakis, F. Brilot, S. Amatayakul-Chantler, N. Roth, G. Coppola, P. Schofield, J. Jackson, J. Y. Henry, O. Mazigi, D. Langley, Y. Lu, C. Forster, S. McAllery, V. Mathivanan, C. Fichter, A. C. Hoppe, M. L. Munier, H.-M. Jack, D. Cromer, D. Darley, G. Matthews, D. Christ, D. Khoury, M. Davenport, W. Rawlinson, A. D. Kelleher, S. Turville, SARS-CoV-2 Omicron: Evasion of potent humoral responses and resistance to clinical immunotherapeutics relative to viral variants of concern. medRxiv 2021.12.14.21267772 [Preprint]. 15 December 2021. https://doi.org/10.1101/2021.12.14.21267772.
20. L. A. VanBlargan, J. M. Errico, P. J. Halfmann, S. J. Zost, J. E. Crowe, L. A. Purcell, Y. Kawaoka, D. Corti, D. H. Fremont, M. S. Diamond, An infectious SARS-CoV-2 B.1.1.529 Omicron virus escapes neutralization by therapeutic monoclonal antibodies. *Nat. Med.* **28**, 490–495 (2022).
21. W. Dejnirattisai, J. Huo, D. Zhou, J. Zahradník, P. Supasa, C. Liu, H. M. E. Duyvesteyn, H. M. Ginn, A. J. Mentzer, A. Tuekprakhon, R. Nutalai, B. Wang, A. Dijokaite, S. Khan, O. Avinoam, M. Bahar, D. Skelly, S. Adele, S. A. Johnson, A. Amini, T. G. Ritter, C. Mason, C. Dold, D. Pan, S. Assadi, A. Bellass, N. Omo-Dare, D. Koeckerling, A. Flaxman, D. Jenkin, P. K. Aley, M. Voysey, S. A. C. Clemens, F. G. Naveca, V. Nascimento, F. Nascimento, C. F. da Costa, P. C. Resende, A. Pauvolid-Correa, M. M. Siqueira, V. Baillie, N. Serafin, G. Kwatra, K. Da Silva, S. A. Madhi, M. C. Nunes, T. Malik, P. J. M. Openshaw, J. K. Baillie, M. G. Semple, A. R. Townsend, K. A. Huang, T. K. Tan, M. W. Carroll, P. Klenerman, E. Barnes, S. J. Dunachie, B. Constantinides, H. Webster, D. Crook, A. J. Pollard, T. Lambe; OPTIC Consortium; ISARIC4C Consortium, N. G. Paterson, M. A. Williams, D. R. Hall, E. E. Fry, J. Mongkolsapaya, J. Ren, G. Schreiber, D. I. Stuart, G. R. Screaton, SARS-CoV-2 Omicron-B.1.1.529 leads to widespread escape from neutralizing antibody responses. *Cell* **185**, 467–484.e15 (2022).
22. S. Iketani, L. Liu, Y. Guo, L. Liu, Y. Huang, M. Wang, Y. Luo, J. Yu, M. T. Yin, M. E. Sobieszczyk, Y. Huang, H. H. Wang, Z. Sheng, D. D. Ho, Antibody evasion properties of SARS-CoV-2 omicron sublineages. *Nature* **604**, 553–556 (2022).
23. K. Westendorf, L. Wang, S. Žentelis, D. Foster, P. Vaillancourt, M. Wiggin, E. Lovett, R. van der Lee, J. ö Hendle, A. Pustilnik, J. M. Sauder, L. Kraft, Y. Hwang, R. W. Siegel, J. Chen, B. A. Heinz, R. E. Higgs, N. Kallewaard, K. Jepson, R. Goya, M. A. Smith, D. W. Collins, D. Pellacani, P. Xiang, V. de Puyraimond, M. Ricicova, L. Devorkin, C. Pritchard, A. O'Neill, K. Dalal, P. Panwar, H. Dhupar, F. A. Garces, C. Cohen, J. Dye, K. E. Huie, C. V. Badger, D. Kobasa, J. Audet, J. J. Freitas, S. Hassanali, I. Hughes, L. Munoz, H. C. Palma, B. Ramamurthy, R. W. Cross, T. W. Geisbert, V. Menacherry, K. Lokugamage, V. Borisevich, I. Lanz, L. Anderson, P. Sipahimalani, K. S. Corbett, E. S. Yang, Y. Zhang, W. Shi, T. Zhou, M. Choe, J. Misasi, P. D. Kwong, N. J. Sullivan, B. S. Graham, T. L. Fernandez, C. L. Hansen, E. Falconer, J. R. Mascola, B. E. Jones, B. C. Barnhart, LY-CoV1404 (bebtelovimab) potently neutralizes SARS-CoV-2 variants. bioRxiv 10.1101/2021.04.30.442182 [Preprint]. 4 May 2022. https://doi.org/10.1101/2021.04.30.442182.
24. A. Baum, B. O. Fulton, E. Wloga, R. Copin, K. E. Pascal, V. Russo, S. Giordano, K. Lanza, N. Negron, M. Ni, Y. Wei, G. S. Atwal, A. J. Murphy, N. Stahl, G. D. Yancopoulos, C. A. Kyratsous, Antibody cocktail to SARS-CoV-2 spike protein prevents rapid mutational escape seen with individual antibodies. *Science* **369**, 1014–1018 (2020).
25. C. Hsieh, J. A. Goldsmith, J. M. Schaub, A. M. DiVenere, H. Kuo, K. Javanmardi, K. C. Le, D. Wrapp, A. G. Lee, Y. Liu, C. Chou, P. O. Byrne, C. K. Hjorth, N. V. Johnson, J. Ludes-Meyers, A. W. Nguyen, J. Park, N. Wang, D. Amengor, J. J. Lavinder, G. C. Ippolito, J. A. Maynard, I. J. Finkelstein, J. S. McLellan, Structure-based design of prefusion-stabilized SARS-CoV-2 spikes. *Science* **369**, 1501–1505 (2020).
26. T. N. Starr, A. J. Greaney, S. K. Hilton, D. Ellis, K. H. D. Crawford, A. S. Dingens, M. J. Navarro, J. E. Bowen, M. A. Tortorici, A. C. Walls, N. P. King, D. Veesler, J. D. Bloom, Deep mutational scanning of SARS-CoV-2 receptor binding domain reveals constraints on folding and ACE2 binding. *Cell* **182**, 1295–1310.e20 (2020).
27. A. J. Schmitz, J. S. Turner, Z. Liu, J. Q. Zhou, I. D. Aziati, R. E. Chen, A. Joshi, T. L. Bricker, T. L. Darling, D. C. Adelsberg, C. G. Altomare, W. B. Alsoussi, J. B. Case, L. A. VanBlargan, T. Lei, M. Thapa, F. Amanat, T. Jeevan, T. Fabrizio, J. A. O'Halloran, P. Shi, R. M. Presti, R. J. Webby, F. Krammer, S. P. J. Whelan, G. Bajic, M. S. Diamond, A. C. M. Boon, A. H. Ellebedy, A vaccine-induced public antibody protects against SARS-CoV-2 and emerging variants. *Immunity* **54**, 2159–2166.e6 (2021).
28. M. A. Tortorici, M. Beltramello, F. A. Lempp, D. Pinto, H. V. Dang, L. E. Rosen, M. McCallum, J. Bowen, A. Minola, S. Jaconi, F. Zatta, A. D. Marco, B. Guarino, S. Bianchi, E. J. Lauron, H. Tucker, J. Zhou, A. Peter, C. Havenar-Daughton, J. A. Wojcechowskyj, J. B. Case, R. E. Chen, H. Kaiser, M. Montiel-Ruiz, M. Meury, N. Czudnochowski, R. Spreafico, J. Dillen, C. Ng, N. Sprugasci, K. Culap, F. Benigni, R. Abdelnabi, S. C. Foo, M. A. Schmid, E. Cameroni, A. Riva, A. Gabrieli, M. Galli, M. S. Pizzuto, J. Neyts, M. S. Diamond, H. W. Virgin, G. Snell, D. Corti, K. Fink, D. Veesler, Ultrapotent human antibodies protect against SARS-CoV-2 challenge via multiple mechanisms. *Science* **370**, 950–957 (2020).
29. T. Li, X. Han, C. Gu, H. Guo, H. Zhang, Y. Wang, C. Hu, K. Wang, F. Liu, F. Luo, Y. Zhang, J. Hu, W. Wang, S. Li, Y. Hao, M. Shen, J. Huang, Y. Long, S. Song, R. Wu, S. Mu, Q. Chen, F. Gao, J. Wang, S. Long, L. Li, Y. Wu, Y. Gao, W. Xu, X. Cai, D. Qu, Z. Zhang, H. Zhang, N. Li, Q. Gao, G. Zhang, C. He, W. Wang, X. Ji, N. Tang, Z. Yuan, Y. Xie, H. Yang, B. Zhang, A. Huang, A. Jin, Potent SARS-CoV-2 neutralizing antibodies with protective efficacy against newly emerged mutational variants. *Nat. Commun.* **12**, 6304 (2021).
30. C. Fenwick, P. Turelli, L. Perez, C. Pellaton, L. Esteves-Leuenberger, A. Farina, J. Campos, E. Lana, F. Fiscalini, C. Raclot, F. Pojer, K. Lau, D. Demurtas, M. Descatoire, V. S. Joo, M. Foglierini, A. Noto, R. Abdelnabi, C. S. Foo, L. Vangeel, J. Neyts, W. Du, B. Bosch, G. Veldman, P. Leyssen, V. Thiel, R. LeGrand, Y. Lévy, D. Trono, G. Pantaleo, A highly potent antibody effective against SARS-CoV-2 variants of concern. *Cell Rep.* **37**, 109814 (2021).
31. L. Wang, T. Zhou, Y. Zhang, E. S. Yang, C. A. Schramm, W. Shi, A. Pegu, O. K. Oloniniyi, A. R. Henry, S. Darko, S. R. Narpala, C. Hatcher, D. R. Martinez, Y. Tsybovsky, E. Phung, O. M. Abiona, A. Antia, E. M. Cale, L. A. Chang, M. Choe, K. S. Corbett, R. L. Davis, A. T. DiPiazza, I. J. Gordon, S. H. Hait, T. Hermanus, P. Kgagudi, F. Laboune, K. Leung, T. Liu, R. D. Mason, A. F. Nazzari, L. Novik, S. O'Connell, S. O'Dell, A. S. Olia, S. D. Schmidt, T. Stephens, C. D. Stringham, C. A. Talana, I. Teng, D. A. Wagner, A. T. Widge, B. Zhang, M. Roederer, J. E. Ledgerwood, T. J. Ruckwardt, M. R. Gaudinski, P. L. Moore, N. A. Doria-Rose, R. S. Baric, B. S. Graham, A. B. McDermott, D. C. Douek, P. D. Kwong, J. R. Mascola, N. J. Sullivan, J. Misasi, Ultrapotent antibodies against diverse and highly transmissible SARS-CoV-2 variants. *Science* **373**, eabh1766 (2021).
32. J. Dong, S. J. Zost, A. J. Greaney, T. N. Starr, A. S. Dingens, E. C. Chen, R. E. Chen, J. B. Case, R. E. Sutton, P. Gilchuk, J. Rodriguez, E. Armstrong, C. Gainza, R. S. Nargi, E. Binshtein, X. Xie, X. Zhang, P. Shi, J. Logue, S. Weston, M. E. McGrath, M. B. Frieman, T. Brady, K. M. Tuffy, H. Bright, Y. Loo, P. M. McTamney, M. T. Esser, R. H. Carnahan, M. S. Diamond, J. D. Bloom, J. E. Crowe Jr., Genetic and structural basis for SARS-CoV-2 variant neutralization by a two-antibody cocktail. *Nat. Microbiol.* **6**, 1233–1244 (2021).
33. V. Dussupt, R. S. Sankhala, L. Mendez-Rivera, S. M. Townsley, F. Schmidt, L. Wieczorek, K. G. Lal, G. C. Donofrio, U. Tran, N. D. Jackson, W. I. Zaky, M. Zemil, S. R. Tritsch, W. Chen, E. J. Martinez, A. Ahmed, M. Choe, W. C. Chang, A. Hajduczki, N. Jian, C. E. Peterson, P. A. Rees, M. Rutkowska, B. M. Slike, C. N. Selverian, I. Swafford, I. Teng, P. V. Thomas, T. Zhou, C. J. Smith, J. R. Currier, P. D. Kwong, M. Rolland, E. Davidson, B. J. Doranz, C. N. Mores, T. Hatziioannou, W. W. Reiley, P. D. Bieniasz, D. Paquin-Proulx, G. D. Gromowski, V. R. Polonis, N. L. Michael, K. Modjarrad, M. G. Joyce, S. J. Krebs, Low-dose in vivo protection and neutralization across SARS-CoV-2 variants by monoclonal antibody combinations. *Nat. Immunol.* **22**, 1503–1514 (2021).

34. Z. Liu, L. A. VanBlargan, L. Bloyet, P. W. Rothlauf, R. E. Chen, S. Stumpf, H. Zhao, J. M. Errico, E. S. Theel, M. J. Liebeskind, B. Alford, W. J. Buchser, A. H. Ellebedy, D. H. Fremont, M. S. Diamond, S. P. J. Whelan, Identification of SARS-CoV-2 spike mutations that attenuate monoclonal and serum antibody neutralization. *Cell Host Microbe* **29**, 477–488.e4 (2021).
35. D. M. Weinreich, S. Sivapalasingam, T. Norton, S. Ali, H. Gao, R. Bhore, B. J. Musser, Y. Soo, D. Rofail, J. Im, C. Perry, C. Pan, R. Hosain, A. Mahmood, J. D. Davis, K. C. Turner, A. T. Hooper, J. D. Hamilton, A. Baum, C. A. Kyratsous, Y. Kim, A. Cook, W. Kampman, A. Kohli, Y. Sachdeva, X. Graber, B. Kowal, T. DiCioccio, N. Stahl, L. Lipsich, N. Braunstein, G. Herman, G. D. Yancopoulos; Trial Investigators, REGN-COV2, a neutralizing antibody cocktail, in outpatients with Covid-19. *N. Engl. J. Med.* **384**, 238–251 (2021).
36. A. Gupta, Y. Gonzalez-Rojas, E. Juarez, M. Crespo Casal, J. Moya, D. R. Falci, E. Sarkis, J. Solis, H. Zheng, N. Scott, A. L. Cathcart, C. M. Hebner, J. Sager, E. Mogalian, C. Tipple, A. Peppercorn, E. Alexander, P. S. Pang, A. Free, C. Brinson, M. Aldinger, A. E. Shapiro; COMET-ICE Investigators, Early treatment for Covid-19 with SARS-CoV-2 neutralizing antibody sotrovimab. *N. Engl. J. Med.* **385**, 1941–1950 (2021).
37. A. E. Shapiro, R. A. Bender Ignacio, Time to knock monoclonal antibodies off the platform for patients hospitalised with COVID-19. *Lancet Infect. Dis.* **22**, 567–569 (2021).
38. C. H. GeurtsvanKessel, D. Geers, K. S. Schmitz, A. Z. Mykytyn, M. M. Lamers, S. Bogers, L. Gommers, R. S. G. Sablerolles, N. N. Nieuwkoop, L. C. Rijsbergen, L. L. A. van Dijk, J. de Wilde, K. Alblas, T. I. Breugem, B. J. A. Rijnders, H. de Jager, D. Weiskopf, P. H. M. van der Kuy, A. Sette, M. P. G. Koopmans, A. Grifoni, B. L. Haagmans, R. D. de Vries, Divergent SARS CoV-2 Omicron-specific T- and B-cell responses in COVID-19 vaccine recipients. *Sci. Immunol.* **7**, eabo2202 (2022).
39. C. Wang, R. van Haperen, J. Gutiérrez-Álvarez, W. Li, N. M. A. Okba, I. Albulescu, I. Widjaja, B. van Dieren, R. Fernandez-Delgado, I. Sola, D. L. Hurdiss, O. Daramola, F. Grosveld, F. J. M. van Kuppeveld, B. L. Haagmans, L. Enjuanes, D. Drabek, B. Bosch, A conserved immunogenic and vulnerable site on the coronavirus spike protein delineated by cross-reactive monoclonal antibodies. *Nat. Commun.* **12**, 1715 (2021).
40. C. Wang, W. Li, D. Drabek, N. M. A. Okba, R. van Haperen, A. D. M. E. Osterhaus, F. J. M. van Kuppeveld, B. L. Haagmans, F. Grosveld, B.-J. Bosch, A human monoclonal antibody blocking SARS-CoV-2 infection. *Nat Commun.* **11**, 2251 (2020).
41. I. Widjaja, C. Wang, R. van Haperen, J. Gutiérrez-Álvarez, B. van Dieren, N. M. A. Okba, V. S. Raj, W. Li, R. Fernandez-Delgado, F. Grosveld, F. J. M. van Kuppeveld, B. L. Haagmans, L. Enjuanes, D. Drabek, B.-J. Bosch, Towards a solution to MERS: Protective human monoclonal antibodies targeting different domains and functions of the MERS-coronavirus spike glycoprotein. *Emerg. Microbes Infect.* **8**, 516–530 (2019).
42. J. Hansen, A. Baum, K. E. Pascal, V. Russo, S. Giordano, E. Wloga, B. O. Fulton, Y. Yan, K. Koon, K. Patel, K. M. Chung, A. Hermann, E. Ullman, J. Cruz, A. Rafique, T. Huang, J. Fairhurst, C. Libertiny, M. Malbec, W. Lee, R. Welsh, G. Farr, S. Pennington, D. Deshpande, J. Cheng, A. Watty, P. Bouffard, R. Babb, N. Levenkova, C. Chen, B. Zhang, A. R. Hernandez, K. Saotome, Y. Zhou, M. Franklin, S. Sivapalasingam, D. C. Lye, S. Weston, J. Logue, R. Haupt, M. Frieman, G. Chen, W. Olson, A. J. Murphy, N. Stahl, G. D. Yancopoulos, C. A. Kyratsous, Studies in humanized mice and convalescent humans yield a SARS-CoV-2 antibody cocktail. *Science* **369**, 1010–1014 (2020).
43. D. Pinto, Y. Park, M. Beltramello, A. C. Walls, M. A. Tortorici, S. Bianchi, S. Jaconi, K. Culap, F. Zatta, A. De Marco, A. Peter, B. Guarino, R. Spreafico, E. Cameroni, J. B. Case, R. E. Chen, C. Havenar-Daughton, G. Snell, A. Telenti, H. W. Virgin, A. Lanzavecchia, M. S. Diamond, K. Fink, D. Veesler, D. Corti, Cross-neutralization of SARS-CoV-2 by a human monoclonal SARS-CoV antibody. *Nature* **583**, 290–295 (2020).
44. M. Yuan, N. C. Wu, X. Zhu, C. D. Lee, R. T. Y. So, H. Lv, C. K. P. Mok, I. A. Wilson, A highly conserved cryptic epitope in the receptor binding domains of SARS-CoV-2 and SARS-CoV. *Science* **368**, 630–633 (2020).
45. J. Zivanov, T. Nakane, B. O. Forsberg, D. Kimanius, W. J. Hagen, E. Lindahl, S. H. Scheres, New tools for automated high-resolution cryo-EM structure determination in RELION-3. *eLife* **7**, e42166 (2018).
46. A. Punjani, J. L. Rubinstein, D. J. Fleet, M. A. Brubaker, cryoSPARC: Algorithms for rapid unsupervised cryo-EM structure determination. *Nat. Methods* **14**, 290–296 (2017).
47. A. Punjani, H. Zhang, D. J. Fleet, Non-uniform refinement: Adaptive regularization improves single-particle cryo-EM reconstruction. *Nat. Methods* **17**, 1214–1221 (2020).
48. E. F. Pettersen, T. D. Goddard, C. C. Huang, G. S. Couch, D. M. Greenblatt, E. C. Meng, T. E. Ferrin, UCSF Chimera—A visualization system for exploratory research and analysis. *J. Comput. Chem.* **25**, 1605–1612 (2004).
49. R. Sanchez-Garcia, J. Gomez-Blanco, A. Cuervo, J. M. Carazo, C. O. S. Sorzano, J. Vargas, DeepEMhancer: A deep learning solution for cryo-EM volume post-processing. *Commun. Biol.* **4**, 874 (2021).
50. M. A. Cianfrocco, M. Wong-Barnum, C. Youn, R. Wagner, A. Leschziner, COSMIC2: A science gateway for cryo-electron microscopy structure determination, in *Proceedings of the Practice and Experience in Advanced Research Computing 2017 on Sustainability, Success and Impact* (ACM, 2017), pp. 1–5.
51. P. Emsley, K. Cowtan, Coot: Model-building tools for molecular graphics. *Acta Crystallogr. D Biol. Crystallogr.* **60**, 2126–2132 (2004).
52. A. Rosa, V. E. Pye, C. Graham, L. Muir, J. Seow, K. W. Ng, N. J. Cook, C. Rees-Spear, E. Parker, M. S. Dos Santos, C. Rosadas, A. Susana, H. Rhys, A. Nans, L. Masino, C. Roustan, E. Christodoulou, R. Ulferts, A. G. Wrobel, C. Short, M. Fertleman, R. W. Sanders, J. Heaney, M. Spyer, S. Kjær, A. Riddell, M. H. Malim, R. Beale, J. I. MacRae, G. P. Taylor, E. Nastouli, M. J. van Gils, P. B. Rosenthal, M. Pizzato, M. O. McClure, R. S. Tedder, G. Kassiotis, L. E. McCoy, K. J. Doores, P. Cherepanov, SARS-CoV-2 can recruit a heme metabolite to evade antibody immunity. *Sci. Adv.* **7**, eabg7607 (2021).
53. J. Lan, J. Ge, J. Yu, S. Shan, H. Zhou, S. Fan, Q. Zhang, X. Shi, Q. Wang, L. Zhang, X. Wang, Structure of the SARS-CoV-2 spike receptor-binding domain bound to the ACE2 receptor. *Nature* **581**, 215–220 (2020).
54. L. A. Kelley, S. Mezulis, C. M. Yates, M. N. Wass, M. J. E. Sternberg, The Phyre2 web portal for protein modeling, prediction and analysis. *Nat. Protoc.* **10**, 845–858 (2015).
55. P. Emsley, M. Crispin, Structural analysis of glycoproteins: Building N-linked glycans with Coot. *Acta Crystallogr. D Struct. Biol.* **74**, 256–263 (2018).
56. J. J. Headd, N. Echols, P. V. Afonine, R. W. Grosse-Kunstleve, V. B. Chen, N. W. Moriarty, D. C. Richardson, J. S. Richardson, P. D. Adams, Use of knowledge-based restraints in phenix.refine to improve macromolecular refinement at low resolution. *Acta Crystallogr. D Biol. Crystallogr.* **68**, 381–390 (2012).
57. V. B. Chen, W. B. Arendall, J. J. Headd, D. A. Keedy, R. M. Immormino, G. J. Kapral, L. W. Murray, J. S. Richardson, D. C. Richardson, MolProbity: All-atom structure validation for macromolecular crystallography. *Acta Crystallogr. D Biol. Crystallogr.* **66**, 12–21 (2010).
58. B. A. Barad, N. Echols, R. Y. Wang, Y. Cheng, F. DiMaio, P. D. Adams, J. S. Fraser, EMRinger: Side chain-directed model and map validation for 3D cryo-electron microscopy. *Nat. Methods* **12**, 943–946 (2015).
59. J. Agirre, J. Iglesias-Fernández, C. Rovira, G. J. Davies, K. S. Wilson, K. D. Cowtan, Privateer: Software for the conformational validation of carbohydrate structures. *Nat. Struct. Mol. Biol.* **22**, 833–834 (2015).
60. J. Agirre, G. Davies, K. Wilson, K. Cowtan, Carbohydrate anomalies in the PDB. *Nat. Chem. Biol.* **11**, 303 (2015).
61. E. Krissinel, K. Henrick, Inference of macromolecular assemblies from crystalline state. *J. Mol. Biol.* **372**, 774–797 (2007).
62. R. A. Laskowski, M. B. Swindells, LigPlot^{+}: Multiple ligand–protein interaction diagrams for drug discovery. *J. Chem. Inf. Model.* **51**, 2778–2786 (2011).
63. T. D. Goddard, C. C. Huang, E. C. Meng, E. F. Pettersen, G. S. Couch, J. H. Morris, T. E. Ferrin, UCSF ChimeraX: Meeting modern challenges in visualization and analysis. *Protein Sci.* **27**, 14–25 (2018).
64. A. Morin, B. Eisenbraun, J. Key, P. C. Sanschagrin, M. A. Timony, M. Ottaviano, P. Sliz, Collaboration gets the most out of software. *eLife* **2**, e01456 (2013).
65. D. K. Meyerholz, J. C. Sieren, A. P. Beck, H. A. Flaherty, Approaches to evaluate lung inflammation in translational research. *Vet. Pathol.* **55**, 42–52 (2018).
66. F. Armando, G. Beythien, F. Kaiser, L. Allnoch, L. Heydemann, M. Rosiak, S. Becker, M. Gonzalez-Hernandez, M. Lamers, B. Haagmans, K. Guilfoyle, G. V. Amerongen, M. Ciurkiewicz, A. Osterhaus, W. Baumgärtner, SARS-CoV-2 Omicron variant causes mild pathology in the upper and lower respiratory tract of Syrian golden hamsters (*Mesocricetus auratus*). *Nat. Commun.* **13**, 3519 (2022).
67. K. Becker, G. Beythien, N. de Buhr, S. Stanelle-Bertram, B. Tuku, N. M. Kouassi, S. Beck, M. Zickler, L. Allnoch, G. Gabriel, M. von Köckritz-Blickwede, W. Baumgärtner, Vasculitis and neutrophil extracellular traps in lungs of golden syrian hamsters with SARS-CoV-2. *Front. Immunol.* **12**, 640842 (2021).
68. B. Bošnjak, I. Odak, J. Barros-Martins, I. Sandrock, S. I. Hammerschmidt, M. Permanyer, G. E. Patzer, H. Greorgiev, R. G. Jauregui, A. Tscherne, J. H. Schwarz, G. Kalodimou, G. Ssebyatika, M. Ciurkiewicz, S. Willenzon, A. Bubke, J. Ristenpart, C. Ritter, T. Tuchel, C. M. Z. Natrup, D. Shin, S. Clever, L. Limpinsel, W. Baumgärtner, T. Krey, A. Volz, G. Sutter, R. Förster, Intranasal delivery of MVA vector vaccine induces effective pulmonary immunity against SARS-CoV-2 in rodents. *Front. Immunol.* **12**, 772240 (2021).

Acknowledgments: We thank C. Schütz, J. Baskas, J.-S. Harre, V. Nijman, M. Chatziandreou, and R. Brouwer for technical support. This study was done within the framework of the Utrecht Molecular Immunology Hub–Utrecht University and the research programme of the Netherlands Centre for One Health (www.ncoh.nl). We thank all members of the MANCO consortium for their valuable input throughout the study. **Funding:** The MANCO project has received funding from the European Union's Horizon 2020 research and innovation programme under grant agreement no. 101003651). This work made use of the Dutch national e-infrastructure with the support of the SURF Cooperative using grant no. EINF-2453. This research was funded by the Deutsche Forschungsgemeinschaft (DFG; German Research Foundation) 398066876/GRK 2485/1; BMBF (Federal Ministry of Education and Research) project entitled RAPID (Risk assessment in re-pandemic respiratory infectious diseases), 01KI1723G; and Ministry of Science and Culture of Lower Saxony in Germany (14-76103-184 CORONA-15/20). **Author contributions:** Gene cloning, protein expression, and purification: W.D., J.v.d.L., T.S., R.v.H., and D.D. Immunization, hybridoma fusion and screening, subcloning,

sequencing, production, and purification: R.v.H. and D.D. Affinity measurements, epitope binning, and neutralization assays: W.D., J.v.d.L., A.Z.M., and M.M.L. Cryo-EM grid preparation and data collection: I.D. Cryo-EM data processing, atomic modeling and interpretation: D.L.H. Animal experiments: M.G.-H., F.K.K., and G.v.A. Pathological investigation: F.A., G.B., M.C., and W.B. Supervision: D.L.H., F.J.M.v.K., B.L.H., L.E., A.D.M.E.O., F.G., and B.-J.B. Study conception and coordination: F.G. and B.-J.B. Manuscript writing: W.D., D.L.H., and B.-J.B., with input from all other authors. **Competing interests:** D.D., R.v.H., and F.G. are (part) employees of Harbour Biomed and may hold company shares. A patent has been filed in the United Kingdom (2112933.3) on the antibody described in this manuscript with F.G., B.L.H., and B.-J.B. as inventors. I.D. is an employee of Thermo Fisher Scientific and may hold company shares. A.D.M.E.O. is the CSO of CR2O, the chair of the ESWI, and the chair of Viroclinics Biosciences DDL and has been an ad hoc consultant or speaker for F. Hoffmann-La Roche Ltd., Sanofi Pasteur, and Janssen Pharmaceuticals. The remaining authors declare that they have no competing interests. **Data and materials availability:** The globally and locally refined cryo-EM maps have been deposited to the Electron Microscopy Data Bank under the accession codes EMD-14250 and EMD-14271, respectively. The atomic model of the 87G7-bound spike has been deposited to the PDB under the accession code 7R40. Materials generated in this study are available on reasonable request. All data needed to evaluate the conclusions in the paper are present in the paper or the Supplementary Materials.

Submitted 7 March 2022
Accepted 19 April 2022
Published First Release 26 April 2022
Final published 29 July 2022
10.1126/sciimmunol.abp9312

Science Immunology

An ACE2-blocking antibody confers broad neutralization and protection against Omicron and other SARS-CoV-2 variants of concern

Wenjuan Du, Daniel L. Hurdiss, Dubravka Drabek, Anna Z. Mykytyn, Franziska K. Kaiser, Mariana Gonzlez-Hernndez, Diego Muoz-Santos, Mart M. Lamers, Rien van Haperen, Wentao Li, Ieva Drulyte, Chunyan Wang, Isabel Sola, Federico Armando, Georg Beythien, Malgorzata Ciurkiewicz, Wolfgang Baumgrtner, Kate Guilfoyle, Tony Smits, Joline van der Lee, Frank J. M. van Kuppeveld, Geert van Amerongen, Bart L. Haagmans, Luis Enjuanes, Albert D. M. E. Osterhaus, Frank Grosveld, and Berend-Jan Bosch

Sci. Immunol., **7** (73), eabp9312.
DOI: 10.1126/sciimmunol.abp9312

Therapeutic antibody neutralizes Omicron

The Omicron variant of SARS-CoV-2 has multiple mutations in the spike protein, facilitating its ability to evade antibodies toward prior variants of concern (VOCs). This has resulted in the loss of efficacy of multiple antibody therapies against SARS-CoV-2 infection. Here, Du *et al.* identified and humanized a monoclonal antibody, 87G7, that potently neutralized all SARS-CoV-2 VOCs, including Omicron BA.1 and BA.2. They identified the specific interactions that the antibody has with the RBD region of Omicron, showing that the antibody can overcome various RBD mutations. Last, 87G7 therapeutically and prophylactically protected mice and hamsters from multiple SARS-CoV-2 VOCs, including Omicron BA.1. Thus, the authors found a monoclonal antibody that might offer clinical benefit for Omicron infection.